Review

TiO_2 photocatalyst for removal of volatile organic compounds in gas phase – A review

Zahra Shayegan, Chang-Seo Lee, Fariborz Haghighat

PII: S1385-8947(17)31652-2
DOI: https://doi.org/10.1016/j.cej.2017.09.153
Reference: CEJ 17738

To appear in: *Chemical Engineering Journal*

Received Date: 16 August 2017
Revised Date: 22 September 2017
Accepted Date: 24 September 2017

Please cite this article as: Z. Shayegan, C-S. Lee, F. Haghighat, TiO_2 photocatalyst for removal of volatile organic compounds in gas phase – A review, *Chemical Engineering Journal* (2017), doi: https://doi.org/10.1016/j.cej.2017.09.153

TiO_2 photocatalyst for removal of volatile organic compounds in gas phase – A review

Zahra Shayegan, Chang-Seo Lee and Fariborz Haghighat*

Department of Building, Civil and Environmental Engineering
Concordia University, Montreal, Quebec, H3G 1M8 CANADA

Abstract

Heterogeneous photocatalytic oxidation process (PCO) is a promising technology for removing indoor volatile organic compounds (VOCs) contaminants. Titanium dioxide (TiO_2) has been regarded as the most suitable photocatalyst for its cost effectiveness, high stability and great capability to degrade various VOCs. However, no TiO_2-based photocatalysts completely satisfy all practical requirements given photoexcited charge carriers' short lifetime and a wide band gap requiring ultraviolet (UV) radiation. Strategies for improving TiO_2 photocatalyst activities by doping with different metal and/or non-metal ions and by coupling with other semiconductors have been examined and reported. These techniques can improve PCO performance through the following mechanisms: i) by introducing an electron capturing level in the band gap that would generate some defects in the TiO_2 lattice and help capture charge carriers; ii) by slowing down the charge carrier recombination rate and increasing VOCs degradation. This paper reports the outcomes of a comprehensive literature review of TiO_2 modification techniques that include approaches for overcoming the inherent TiO_2 limitations and improving the photocatalytic degradation of VOCs. Accordingly, it focuses on the recent development of modified-TiO_2 used for degrading gas phase pollutants in ambient conditions. Modification techniques, such as metal and non-metal doping, co-doping, and the heterojunction of TiO_2 with other semiconductors, are reviewed. A brief introduction on the basics of photocatalysis and the effects of controlling parameters is presented, followed by a discussion about TiO_2 photocatalyst modification for gas phase applications. The reported experimental results obtained with PCO for eliminating VOCs are also compiled and evaluated.

Keywords: Volatile organic compounds (VOCs), Photocatalytic oxidation (PCO), Titanium dioxide (TiO_2), TiO_2 modification, Doping, Composite.

* Corresponding Author: Fariborz.Haghighat@Concordia.ca

Contents

1. Introduction

Volatile organic compounds (VOCs) are a major group of biogenic/anthropogenic indoor air pollutants with several proven adverse health effects [1]. VOCs are not only hazardous compounds, but also participate in undesirable mechanisms with harmful by-products, including organic compounds, ozone, and secondary organic aerosols [2]. To solve this problem, several air purification techniques have been proposed for VOCs removal [3, 4]. Based on the literature, photocatalyst oxidation (PCO) is a promising VOCs removal method [5, 6].

In PCO, VOCs destruction is conducted by using photocatalysts and UV light at ambient temperature [7, 8]. Common photocatalysts (semiconductor materials) used in PCO are TiO_2, ZnO, WO_3, ZnS, and CdS [9, 10]. Up to now, the application of titanium dioxide (TiO_2) for photodegradation of organic contaminates [11-13] as well as batteries and solar cells [14-17] has generated significant attention due to its unique characteristics and environmental friendliness. Additionally, this option is attractive given TiO_2 low cost, simple preparation, high stability, and great capability to degrade various VOCs pollutants [18-20]. Despite its merits, there are some drawbacks, including the large band gap and high charge carrier recombination rate, which restrict its application under visible light or natural solar light irradiation. Given the wide band gap, the electron from TiO_2 valence band can only be activated under ultraviolet (UV) radiation. Furthermore, the quick recombination of photogenerated electrons and holes reduces photonic efficiency and consequently PCO efficiency as well. Therefore, it is imperative to develop highly efficient photocatalysts that separate charge carriers, slow down their recombination rate, and can also be excited under visible irradiation.

Moreover, to enhance the quantum yield of TiO_2 under visible light irradiation, two obstacles must be overcome—the generation of photoexcited charge carriers must be enhanced, and the separation efficiency of these photogenerated charge carriers improved [21-24].

Significant efforts have been made to overcome the aforementioned disadvantages via various strategies such as metal or non-metal doping, co-doping, and coupling with other semiconductors. These techniques seem effective for increasing the lifetime of the photoexcited pairs of charge carriers and for shifting the band gap absorption edges to the visible range of irradiation light [22, 25, 26]. Based on our knowledge, despite considerable reported research on modifying TiO_2-based photocatalysts, there is a lack of a comprehensive review regarding the

effect of modifying TiO_2 by dopants on the removal performance of VOCs in PCO processes in the gas phase. Here, we have provided a comprehensive literature review of TiO_2 modification to present the approaches required for overcoming the inherent TiO_2 limitations and improving the photocatalytic degradation of VOCs. Accordingly, this paper discusses modification techniques. Such techniques include using metal and non-metal dopants, co-doped ions, and composite TiO_2 with other semiconductors for photocatalytic degradation of pollutants in the gas phase. This paper also summarizes the effects of controlling parameters such as relative humidity, air flow rate, UV light, and initial contaminate concentration on VOCs decomposition with TiO_2 photocatalysts.

2. Basic principles of photocatalytic oxidation process

Photocatalyst reactions begin when an electron is stimulated with light energy equal to or greater than the semiconductor's band gap (Fig. 1) [27]. Transferring a photoexcited electron from the valence band (VB) to the conduction band (CB) leaves a hole in the latter, which can be a powerful oxidizing agent. Consequently, electron and hole pairs (e^-/h^+) are produced [28-30]. These

pairs can be generated in femtoseconds (fs). Afterwards, photoexcited charge carriers can be trapped within picoseconds (ps) (shallow trap) or nanoseconds (ns) (deep trap) [31]. The hole and electron can recombine in a few tens of nanoseconds [32, 33].

(Figure 1)

Environmental applications of semiconductor photocatalysts are directly related to the interfacial charge transfer mechanism between the semiconductor surface and organic compounds. Furthermore, the mechanism and time scale of interfacial charge transfers and recombination charge carriers could be affected by the interface structure [34, 35]. Moreover, trapped photoexcited holes and electrons exist for nanoseconds and microseconds (μs), respectively [32, 33]. Interfacial charge transfers might oxidize or reduce pollutants directly or produce reactive oxidants like hydroxyl radicals and superoxides [36, 37]. For TiO_2, UV light (about 3% of solar radiation) is a common energy source for PCO because of its wide band gap [38].

The minimum band gap energy required for a photon to generate charge carriers over a TiO_2 semiconductor (anatase phase) is 3.2 eV. This is equivalent to the absorption of a 388 nm wavelength photon. Therefore, TiO_2 photoactivation occurs in $\lambda < 388$ nm, near the UV region [9, 28]. Recently, some researchers have modified TiO_2 to enhance its photoactivity under visible light irradiation [39, 40]. Several studies reported that TiO_2 crystalline form affects its photocatalytic activity [41-43]. TiO_2 has three stable polymorphs—anatase (E_g = 3.2 eV), rutile (E_g = 3.02 eV), and brookite (E_g = 3.14 eV) [10, 44]. For PCO, the anatase performs better than the rutile because its conduction band location drives conjugate reactions involving electrons more efficiently[45]. Combining the rutile and anatase phases has been recommended for increasing TiO_2 photocatalytic activity [27, 43]. Given these facts, Degussa P25 TiO_2, composed of 75% anatase and 25% rutile, is a commonly-used commercial catalyst [27].

To reduce the recombination rate, it is essential that electron acceptors and photogenerated electrons react [46]. When appropriate surface electron acceptors or a surface defect state are absent, and thus unavailable to trap these charge carriers, electrons and holes pair in a few nanoseconds, reducing the efficiency of photocatalytic degradation. It is reported that the anatase conduction band edge exceeds the rutile by 0.2 eV. This difference facilitates the electron transfer via an electron bridge [47]. As a result, the electron based on the anatase conduction band jumps to the less positive rutile part, thereby reducing the recombination rate of electrons and the formation of positive holes in the anatase site [41, 48].

Using nanocatalysts helps produced electrons reach the surface and react with electron acceptors in a shorter transfer distance. Therefore, the nanostructure recombination rate is lower than the microstructure [46]. Different TiO_2 nanostructure materials such as nanorods, nanofibers, nanospheres, nanosheets, and nanotubes have been produced in the nanostructure, which proves its efficiency [49]. It is proven that various parameters, such as crystallite size, specific surface area, pore structure, pore volume, and crystalline phases, have significant effects on photocatalytic performance [50]. The nano-sized catalyst high surface area and high surface density improves catalyst performance and photoactivity [49, 51].

In general, several factors influence PCO efficiency, such as humidity, flow rate, the initial concentration of contaminant, the characteristics of the photocatalyst, light source, etc. [7, 8]. The effects of above-mentioned parameters are reviewed briefly in Section 4.

3. Issues in VOCs photocatalytic oxidation

For key reactions involved in photocatalytic oxidation, see Table 1. Equation 1 (Photoexcitation) explains TiO_2 activation by UV light [10, 52]. The $HOO^{\bullet}$ in Eq. (5) is an electron acceptor that produces hydrogen peroxide (H_2O_2). This generates H_2O_2 as an oxidizing agent and decreases the recombination rate of electrons and holes by capturing photo-induced electrons, thereby enhancing PCO efficiency (Eqs. (6-7)). Reduction and oxidation reactions can both occur on the surface of the photoexcited semiconductor. The main oxidant species for degrading VOCs are hydroxyl radicals produced by oxidizing adsorbed water or adsorbed OH^-. The final results of total mineralization of hydrocarbon compounds by PCO are CO_2 and H_2O [10, 40].

(Table 1)

Photocatalytic oxidation of VOCs includes several processes such as the formation and recombination of electrons and holes, the adsorption of VOCs, chemical degradation, and the desorption of products or intermediates [20]. Moreover, photogenerated electrons and holes may take several pathways. They may recombine on the surface or in the bulk of the semiconductor; electron acceptors may be reduced by electrons; electron donors could be oxidized by holes. Photogenerated electrons and holes could react with O_2 and H_2O to produce reactive oxygen species (ROS) [27]. As mentioned above, most holes are then consumed by reacting directly with adsorbed organic materials or adsorbed water molecules [50]. In some PCO reactions, partial mineralization of parent pollutants can generate some by-products. These intermediates can occupy the catalyst active site and decrease catalyst photoactivity [53].

4. Factors affecting PCO performance

This paper briefly reviews the effects of relative humidity, airflow rate, UV light, and the initial contaminate concentration of VOCs photodegradation. These parameters were also reviewed by Mamaghani [54].

4.1. Relative humidity (RH)

In PCO, the presence of water vapor can be both beneficial and detrimental. Water molecules contribute to photocatalytic oxidation process both as competitive adsorbents and resources for

hydroxyl radicals. The resulting hydroxyl radicals are key players in the oxidation process (Eq. 2). In addition, water vapors can be adsorbed on TiO_2 active sites. This reduces the adsorption of VOCs compounds. Therefore, it is clear that changes in relative humidity (RH) can significantly impact photocatalytic oxidation efficiency [10, 52, 55-59]. Water makes photocatalytic degradation more efficient for some contaminants, like benzene and toluene [56]. In other words, complete mineralization of some pollutants to CO_2 is impossible without water vapor. However, excessive water concentration causes the adsorption of water molecules on the active sites of the catalyst surface and decreases the reaction rate [7, 53, 60, 61]. There are few studies on the effect of relative humidity on doped TiO_2 for gas phase pollutants [39, 62-65]. Earlier studies focused only on the effect of relative humidity on the reaction mechanism of different pollutants. Doped TiO_2 performance with different amounts of dopants in humid conditions has not been thoroughly investigated. Doped TiO_2 could improve photocatalytic efficiency more than undoped TiO_2 in the same humidity. Additionally, the doped TiO_2 catalyst could reduce competition between target compound and water adsorption since the increased separation of electrons and holes produces more oxidizing agents.

4.2. Airflow rate

The airflow rate is a key factor for the photocatalytic oxidation of VOCs. Generally, increasing the airflow rate has two adversary effects. First, reducing residence time during PCO decreases pollutants photodegradation efficiency. Second, increasing the mass transfer rate between the contaminants and catalyst improves the conversion rate [41, 66-68]. Therefore, decreasing the airflow rate increases residence time and gives more VOCs contaminants the chance of being adsorbed on the surface of the catalyst. More adsorbed molecules react with hydroxyl radicals or photo-induced holes and then degrade [7]. According to Han et al. [66] and Yang et al. [67], an increase in flow rate causes a higher mass transfer and a smaller concentration gradient between the bulk and the catalyst surface in laminar regimes. In transitional conditions, the oxidation rate depends on both gas-phase mass transfer rates and surface reactions. It has been reported that the effect of airflow rate on VOCs removal falls under three distinct regimes. [56]. In low airflow rates, increasing the airflow rate enhances VOCs removal. This demonstrates that mass transfer to the catalyst surface limits VOCs elimination. In intermediate airflow rates, flow rate variation has no considerable effect on VOCs removal. This means that surface reaction kinetics is the controlling stage. Finally, in high airflow rates, an increased airflow rate decreases the residence

time for transferring VOCs contaminants from the gas phase to the catalyst surface, thereby decreasing the VOCs removal rate.

4.3. UV light intensity and type

It is worth noting that light intensity is one crucial factor for influencing VOCs reaction rate. Generally, photocatalytic oxidation performance enhances when light intensity increases [10, 69]. Augmenting UV light intensity creates more photons, which provide degradation energy [7]. In general, increasing light intensity augments the production of oxidant species. Moreover, increasing the UV-irradiation intensity heightens photoactivity and consequently enhances the photocatalytic degradation of VOCs pollutants [7, 9, 10, 70]. However, energy loss resulting from light reflection, light transmission, or heat is inevitable in PCO. Attempts have been made to use more energy through different methods such as metal and non-metal ion doping, [9, 71-73], coupling with other semiconductors [60, 74], and surface modification [73]. The recombination of charge carriers, and low interfacial charge transfer rates, are responsible for low quantum yields [29, 75]. The overall quantum yield of light absorbed by photocatalysts or reactants can be estimated using the following equation:

$$\Phi_{\text{overall}} = \frac{rate\ of\ reaction}{rate\ of\ absorption\ of\ radiation} \quad (9)$$

where Φ_{overall} is the quantum yield.

Since semiconductors in the heterogeneous medium cannot absorb all refracted irradiation, it is difficult to determine quantum efficiency [9]. Without charge carrier recombination, quantum yield could approach the ideal value of one (1) for UV light with a wavelength small enough to activate the catalyst [76]. VOCs contaminant in the presence of vacuum UV (VUV) lamps can be degraded by photolysis, radical oxidation, and ozonation [77, 78]. Compared with conventional PCO under UV light (254 or 365 nm), VUV light can significantly enhance photocatalytic degradation efficiency. Moreover, by providing a strong oxidation environment and preventing the generation and accumulation of intermediates, VUV light reduces catalyst deactivation [77, 79, 80]. Despite these benefits, performing PCO with VUV lamps produces ozone (O_3) molecules as a by-product. Ozone is a powerful oxidizing species that can react with VOCs pollutants and promote photocatalytic efficiency. However, residual ozone can damage the environment and human health [7, 8, 67, 77, 81].

4.4. Inlet contaminant concentration

The lower initial concentration of contaminants increases removal efficiency in all VOCs. This occurs because the catalyst constant number of active sites has limited adsorption capacity. Furthermore, by-product formation inhibits VOCs adsorption, especially when initial contaminant concentration is high. PCO is therefore more appropriate for photodegrading contaminants in low concentration [7, 82]. The latter can also affect the photocatalyst quantum yield. In fact, when the contaminant is highly concentrated, TiO_2 surface becomes saturated and quantum yield diminishes due to the shielding effect of the contaminant on the catalyst surface [9]. A high concentration of contaminants can also reduce quantum yield by absorbing or scattering light and thus prevent light absorption by the catalyst. Catalyst saturation and competition between adsorbed compounds are higher when inlet contaminants concentration increases [41].

Table 2 provides an overview of TiO_2-based photocatalytic oxidation of various VOCs contaminants and summarizes key operating parameters (e.g. temperature, RH, flow rate, lamp type, and light intensity), maximum conversion, and the main remarks of various studies on VOCs photocatalytic degradation. Accordingly, different types of VOCs, such as alkane, alkene, alcohol, aromatics, ketone, and aldehyde are considered. As Table 2 shows, most studies used UV lamps for all experiments and initial contaminant concentrations were in the range of ppm. One important concern regarding VOCs removal by PCO is the formation of hazardous by-products. Consequently, it is important to modify TiO_2 for VOCs elimination efficiency. Its modification lessens by-product formation, permits the use of TiO_2 under visible light irradiation and allows the removal of indoors contaminants within the range of ppb.

(Table 2)

4.5. Effect of doping

As stated before, TiO_2 photocatalytic efficiency for environmental applications is limited because of charge carriers high recombination rate. TiO_2 photocatalytic activation is also limited under visible light given its wide band gap [86].

Some promising technologies for modifying TiO_2 that can improve environmental pollutants degradation have been proposed. Techniques include doping TiO_2 with metal or non-metal dopants, co-doping TiO_2 with different elements, and coupling TiO_2 with semiconductors with lower band gap energy. These modifications increase charge separation and shift the light absorption range towards visible light [22]. Generally, an appropriate amount of dopants reduces the band gap and consequently allows light absorption at a higher wavelength [48, 71].

Both metal and non-metal doping methods change TiO_2 electronic structure by inducing new doping levels inside its band gap. The doping levels inside TiO_2 band gap can absorb photons in the visible range, expanding the light absorption range by accepting photogenerated electrons from TiO_2 valence band. This reduces charge carriers recombination rate [23, 87].

See Table 3 for a summary of some preparation methods and a characterization analysis of modified catalysts available in the literature. Among preparation methods reported, the sol-gel technique is the most widely used for its ability to synthesize at ambient temperature and pressure. It also provides good adherence to different substrate shapes [59]. In addition, this process is simple and can control the particle size, shape, properties and product chemical composition [10, 88, 89]. Moreover, it can provide TiO_2 appropriate textural properties, including a highly specific surface area and a porous structure—characteristics that enhance photocatalytic efficiency [88].

(Table 3)

5. Different types of TiO_2 doping

5.1. Metal doping TiO_2

Metal doping is used for introducing additional states in the TiO_2 band gap [92]. With less energy transitions required, these impurity levels cause visible light absorption [107]. TiO_2 band gap impurity levels are induced by substituting metal ions for Ti^{4+}, closest to the conduction band. As Fig. 1 shows, electrons can be transferred from the TiO_2 conduction band to doping states, or can be excited from TiO_2 valence band to doping states by photons with energy less than 3.2 eV. In addition, metal doping could improve electron trapping by reducing the electron and hole recombination rate [108-110]. The resulting photocatalytic activity and dopant states energy levels strongly depend on several factors, including the dopant chemical nature, its

concentration, and thermal treatment during photocatalyst preparation [107]. It is evident that each cationic dopant presents individual effects on photoactivity. Therefore, the resulting impact may vary depending on the catalyst preparation method or reaction conditions [111]. In general, the preparation method for doped catalysts creates different crystal properties and changes photocatalyst morphology [93, 112]. The different kinds of metal dopants—noble metals, rare earth metals, and transition metals—and their limitations are reviewed in the following sections.

5.1.1. Noble metal and rare earth metal

Noble metals, such as palladium (Pd) [113], platinum (Pt) [91, 94], silver (Ag) [114], ruthenium (Ru) [95], and iridium (Ir) [96], expand TiO_2 light absorption range to visible light. Unlike most base metals, noble metals are highly resistant to oxidation and corrosion in humid air. In the presence of noble metals, charge carriers recombination decreases, which causes photoactivity on the surface of catalyst to increase [91]. Doping noble metal nanoparticles into TiO_2 lattice effectively retards charge carriers recombination as a result of the Schottky barrier formed at the interface of metal-semiconductor (TiO_2) junction. Reducing the electron and hole recombination rate enhances catalysts photoactivity [91, 115]. In fact, the metal nanoparticles form an intermediary for trapping and transferring photogenerated electrons from the TiO_2 surface to electron acceptors [115].

Rare earth metals are a group of 17 chemical elements, including scandium (Sc), yttrium (Y), and 15 lanthanides, in the periodic table. These metals, having incomplete 4f and empty 5d orbitals, could promote catalysis. It has been reported that incorporating rare earth metal ions into TiO_2 lattice could enhance the adsorption of organic pollutants on the catalyst surface, and thus improve TiO_2 photoactivity [116].

Doped TiO_2 photocatalysts with rare earth cations can enhance photocatalysis by increasing light absorption along with modifications of the phase structure, surface area, and surface morphology. Additionally, during the synthesizing process, doping with rare earth ions inhibits the transition from the anatase phase to the rutile phase [117]. Burns et al [26] described that substitutional incorporation of neodymium ion dopants distorts the TiO_2 lattice because Nd^{3+} ionic radius (0.983 Å) is significantly larger than Ti^{4+} ion (0.605 Å). Li et al. [118] argued that Nd^{3+} ions could not enter in the TiO_2 lattice and replace Ti^{4+} ions; by contrast, Ti^{4+} ions replace lanthanide ions in the lanthanide oxides lattice on the Ln^{3+}-TiO_2 interface, producing a Ti-O-Ln

bond. Consequently, TiO_2 lattice crystallite size decreases, causing some defects in TiO_2. As a result, finding an optimum amount of dopants is critical for obtaining an appropriate number of defects level.

Recently, doping with metals from the lanthanide group (especially Ce-doped TiO_2) has become an attractive approach. According to Xiao et al. [119], mesoporous Ce-doped TiO_2 has a high surface area, high thermal stability in the anatase phase, and better adsorption capacity for VOCs, which could improve contaminants adsorption on the photocatalyst surface. Korologos et al. [113] studied benzene, toluene, ethylbenzene, and xylene (BTEX) PCO in the gas phase using TiO_2-based photocatalysts. They investigated the effects of different dopants (0.25% (w/w) Pt, Fe, and Ce) on photocatalytic performance. The results illustrated that P25/Ce photocatalyst was the most effective catalyst for benzene and ethylbenzene degradation, and showed comparable performance to the P25 for toluene and m-xylene photocatalytic oxidation.

5.1.2. Transition metal

Researchers have investigated the effects of transition metals such as manganese (Mn) [62], iron (Fe) [73, 86, 90], copper (Cu) [63, 110], vanadium (V) [109], and nickel (Ni) [21] on reducing band gap, decreasing electron and hole recombination rate, and using visible light [10, 90]. The type and amount of transition metals are two decisive parameters for PCO. If the amount of metal dopants remains at an optimum level, dopants can increase the separation of electrons and holes by acting as a charge carrier bridge. However, beyond their optimum value, dopants may distort the catalyst crystallinity and act as a recombination center, reducing PCO efficiency [10, 90]. Therefore, further research is needed to determine the optimal type and concentration of dopant. Fig. 2 compares the influence of different amounts of several metal ions on VOCs conversion, and shows that an optimum concentration of dopants enhances pollutants conversion.

(Figure 2)

Moreover, the photocatalyst surface sites can also be occupied by metal ion dopants, which alter the TiO_2 surface properties depending on dopant type and concentration [63, 109].

Iron. Iron (Fe)-doped TiO_2 is the most popular transition metal-functionalized photocatalyst. Doping Fe into TiO_2 structure decreases electron and hole recombination and reduces band gaps

(Fig. 3). Figure 3 demonstrates that Fe doping narrows the band gap and expands light absorption into the visible range [90]. In addition, iron is much cheaper than noble metals such as Pd, Pt, Ag, Au, and Rh, which explains its widespread use [86]. The main reason for promoting Fe-doped TiO_2 as a catalyst is that the Fe^{3+}/Fe^{2+} reduction process enhances charge carrier separation [120]. Fe^{3+} accepts the photoexcited electron, transfers it to the oxygen molecule, and thus produces superoxide [120]. In addition, the radius of Fe^{3+} (0.64 Å) and Ti^{4+} (0.68 Å) is similar, which eases Fe^{3+} ion incorporation into TiO_2 crystal lattice [87, 121]. As a result, Fe ions are distributed uniformly in TiO_2 lattice interstices, which creates defects in TiO_2 structure [121]. The following reactions demonstrated that Fe^{3+} would operate as an electron and hole trap [86, 120]:

$$Fe^{3+} + e^- \rightarrow Fe^{2+} \quad (10)$$

$$Fe^{2+} + O_2 \rightarrow Fe^{3+} + O_2^- \quad (11)$$

$$Fe^{3+} + h^+ \rightarrow Fe^{4+} \quad (12)$$

Therefore, the charge carriers recombination decreases and TiO_2 photoactivity enhances.

(Figure 3)

Yang et al. [86] studied iron-doped TiO_2 for BTEX photodegradation on glass fiber (GF). GF-Fe-TiO_2 composites (at different Fe-to-Ti ratios) showed higher photocatalytic activity for BTEX compared to GF-TiO_2 (as a reference) under visible light irradiation [86]. Tieng et al. [90] reported that Fe^{3+} ions could be trapping sites for both photogenerated conduction band electrons and valence band holes. Consequently, the photogenerated charge carriers could be separated more easily and protected for a longer time. As a result, adsorbed species redox reaction occurs more efficiently.

Fig. 2 shows the effect of different amounts of Fe ions in toluene photodegradation [86, 120, 122]. As this figure demonstrates, the optimal amount of Fe ion is around 0.01 wt.%. Increasing the amount of Fe dopant facilitates the transformation of anatase into rutile and increases the rutile phase [121].

Nickel. When Ni is added to the TiO_2 structure, it traps photogenerated electrons and separates charge carriers, like an electron acceptor. As a result, Ni^{2+} ions could improve TiO_2 photoactivity [123]. Tseng et al. [64] pointed out that the efficient separation of photogenerated electron and hole pairs depends on the concentration of dopant. In contrast, the dopant may become the

recombination center for photogenerated electrons and holes. In low dopant concentration, doped-Ni^{2+} separates charge carriers by trapping electrons. This increases the likelihood of a hole and VOCs reaction. However, in high dopant concentration, doped-Ni^{2+} acts as recombination center preventing hole formation [64]. According to the following equation, Ni^{+} could transfer electrons to the adsorbed O_2 on the surface of TiO_2 (Eq. 15) and react with Ti^{4+} (Eq. 16) to create an interfacial electron transfer [64].

$$TiO_2 + h\vartheta \rightarrow e_{cb}^- + h_{\vartheta b}^+ \quad (13)$$

$$Ni^{2+} + e_{cb}^- \rightarrow Ni^+ \quad (14)$$

$$Ni^+ + O_{2(ads)} \rightarrow Ni^{2+} + O_2^- \quad (15)$$

$$Ni^+ + Ti^{4+} \rightarrow Ni^{2+} + Ti^{3+} \quad (16)$$

$$Ti^{3+} + O_{2(ads)} \rightarrow Ti^{4+} + O_2^- \quad (17)$$

Other transition metals. Huang et al. [79] reported benzene degradation on TiO_2 catalysts with different metal dopants. According to their results, the BET surface area decreased as transition metals (Mn, Co, Cu, Ni, and Fe) were doped in TiO_2 lattice. Transition metals might block TiO_2 pores or cause the particle size to grow, and thus eventually decrease the surface area.

Pham et al. [63] studied benzene photodegradation under visible light on Cu-doped TiO_2, which was supported on porous polyurethane (PU). According to their XPS results, Cu dopants could be substituted by Ti^{4+} ions and generate some defect levels on the TiO_2 lattice by forming Cu-O-Ti bonds. Cu-doping TiO_2 improved charge carriers generation. This was possible due to the production of copper oxides (Cu_2O and CuO), which blend with TiO_2 on the photocatalyst surface. Because these copper oxides possess semiconductor properties, they could generate a number of electron and hole pairs under visible light and enhance the photocatalytic degradation of benzene.

Pham et al. [109] investigated toluene degradation on the surface of V-doped TiO_2/PU photocatalysts. The photocatalyst surface in the presence of water vapor could be hydroxylated and form Ti-OH or V-OH bonds. This can happen through the reaction between water and some cations on a photocatalyst surface, including Ti^{3+}, Ti^{4+}, V^{4+}, and V^{5+} ions.

As presented in Table 4, a cation-doped TiO_2 photocatalyst exhibits enhanced photocatalytic degradation performance compared to that of pure TiO_2 or commercial P25 under both UV and visible light. Accordingly, P25 and undoped TiO_2 have no photoactivity under visible light. In

addition, it is obvious that by increasing the small amount of cation dopants, light absorption in the visible range enhances. Furthermore, all cation-doped catalysts exhibited higher photocatalytic efficiency under UV light than under visible light.

(Table 4)

5.2. Non-metal doping TiO_2

Some other researchers have shown that TiO_2 band gap narrowing can be improved by using non-metal (anion) dopants rather than cations [39, 101]. Various studies show that doping TiO_2 with anionic non-metals—nitrogen (N) [19, 24, 39, 71, 106, 120], carbon (C) [38, 97-99], sulfur (S) [65, 101], boron (B) [23], and fluorine (F) [100]—gives promising results. In non-metal doping, dopant states are near the valence band edge and do not act as charge carriers. Therefore, their role as recombination centers might be minimized [126]. Consequently, anion dopants might be more appropriate than cation dopants for expanding TiO_2 light absorption range into the visible region. As Fig. 1 illustrates, impurity levels caused by doping non-metal dopants into TiO_2 lattice are close to the valence band. For an anion-doped TiO_2, the dopants substitute for oxygen (O_2) in the TiO_2 lattice. This expands its light absorption range and narrows the band gap with non-metal dopants p-orbitals (Fig. 1) [10].

Table 5 summarizes a number of anion-doped TiO_2 photocatalysts synthesized to enhance TiO_2 photocatalytic degradation performance. Accordingly, different non-metal elements were considered. Improvements in photocatalytic degradation were observed after adding a small amount of anion dopants. As Table 5 shows, neither undoped TiO_2 or P25 excite under visible light, like in the cation-doping method. Non-metal dopants could change TiO_2 morphology, and increase its photoactivity performance in PCO [71, 72]. In addition, doping with non-metal anions affects the semiconductor electronic structure [25].

Some researchers have reported that thermal treatment during catalyst synthesis caused changes in the catalyst specific surface area and pore volume, which decreased as temperature rose [72, 98]. A number of studies considered the preparation of non-metal-doping TiO_2 by physical or chemical methods, including sol-gel, hydrothermal, hydrolysis, and microemulsion. Table 3

summarizes some of these methods. As this table illustrates, non-metal doped TiO_2 powders are synthesized by applying different preparation methods and precursors.

C- and N-doped TiO_2 nanomaterials have been demonstrated to have superior photocatalytic activity under visible light irradiation compared to other anion dopants [126]. In the following sections C-, N-, and S- doped TiO_2 along with non-metal doping drawbacks are reviewed.

5.2.1. N-doped

The N-doped TiO_2 has received significant attention because it can narrow the TiO_2 band gap and accelerate the charge carrier transfer process [127]. Furthermore, N-doped TiO_2 changes the hardness, refraction index, electrical conductivity, elastic modulus, and photocatalytic activity in the visible light region [10, 71, 106]. Nitrogen has a low ionization potential and an atomic radius comparable to oxygen, meaning N can easily enter the TiO_2 lattice [128]. According to the literature, a general theory suggests that incorporating non-metal dopants with lower electronegativity than oxygen in the TiO_2 lattice shifts 2p-orbital levels of the valence band upward and results in narrower band gap. However, metal doping leads to additional energy states inside the band gap itself (Fig. 4a) [127, 128].

According to Pandian et al. research [128] on electronic band structures for N-doped TiO_2, the highest localized state (acceptor levels) with substitutional nitrogen is 0.14 eV (above the valence band) and 0.73 eV for interstitial nitrogen (Fig. 4a). The substitutional nitrogen is created by mixing N_{2p} orbitals with TiO_2 O_{2p} orbitals. If the latter produces states above the valence band and narrows the band gap, the former correlated interaction between N_{2p} and Ti_{3d} orbitals forms the mid-gap level of N–O states [88, 128]. One problem of N-doping is the significant energy shift in the valence band gap edge occurring in low concentrations of nitrogen. This indicates that, to extend light absorption and improve photocatalytic activity, it is essential to choose the appropriate preparation techniques for N-doped TiO_2 [71]. Albrbar et al. [88] reported that nitrogen can be incorporated in the TiO_2 lattice structure as a N^{3-} anion interstitially, or by substituting O^{2-} anions [88]. According to Zeng et al. [19] XPS results for N-TiO_2, three peaks are identified for N_{1s}: 396.1 eV, 400 eV, and 403.6 eV. The first N_{1s} peak (396.1 eV) is attributed to the substitutional nitrogen dopant since the 395.6 eV is characteristic of N^{3-} corresponding to the Ti-N bond. The second peak (400 eV) at high binding energies is

attributed to interstitial nitrogen dopants, and the third one (403.6 eV) is usually defined as NOx species. This indicates the successful incorporation of nitrogen into the TiO_2 lattice [19].

5.2.2. C-doped

C-doped TiO_2 can significantly stabilize anatase TiO_2 and enhance the adsorption of organic contaminants on the catalyst surface. It also increases TiO_2 conductivity, which accelerates the charge transfer from inside TiO_2 structure to the surface to participate in oxidation reactions [98, 99]. Di Valentin et al. [129] studied how replacing oxygen sites with carbon, or putting carbon into the interstitial sites of TiO_2 lattice, enhances visible light absorption. There is a debate around carbon-doped TiO_2 similar to that around nitrogen doping on whether the doped type of carbon is substitutional or interstitial. Furthermore, the band gap can also be narrowed with residual carbon-containing species. These have a complex composition given the partial removal of organic compounds in the calcination procedure [126].

As Fig. 4b demonstrates and according to Khalilzade et al. [130], C-doped TiO_2 mid-gap band position shifts upward when carbon concentration increases, which shows a high oxidative potential for photogenerated holes. The new electronic level above TiO_2 valence band was responsible for narrowing C-doped TiO_2 band gap and visible light photoactivity. Wang et al. [99] studied C-doped TiO_2 at different calcination temperatures. They pointed out that C-doping added the deepest states to the band gap compared with N and S-doping (Fig. 4).

Choosing an appropriate method for catalyst preparation is critical for reducing the number of TiO_2 lattice defects. The latter act as great recombination centers for charge carriers and limit the visible light photocatalytic efficiency [98]. Different C-doped TiO_2 preparation methods can be seen in Table 3.

5.2.3. S-doped

S-doped TiO_2 has been investigated extensively in environmental (air and water pollution) uses [101, 131]. Introducing S into the TiO_2 lattice narrows the band gap. Mixing S_{3p} states with O_{2p} of TiO_2 valence band was demonstrated to help increase the valence band width, and narrow the band gap too (Fig. 4c) [131]. S dopant ions can be incorporated into the TiO_2 lattice either as a S^{2-} anion. In S-doping, S^{2-} is replaced with lattice oxygen (O_2), or as a cation, where S^{4+}/S^{6+} substitutes Ti^{4+}. [88, 132]. Ma et al. [131] reported that Ti^{4+} ion atomic radius (0.64 Å) is relatively greater than S^{6+} ion (0.29 Å). Therefore, in S-doped TiO_2 catalyst when S^{6+} substitutes

Ti^{4+} might decrease the catalyst crystal size. Jo et al. [65] reported that TEM images for S-doped TiO_2 show less agglomeration than those of TiO_2 Degussa (un-doped). Furthermore, SEM images of both catalysts illustrate that S-doped TiO_2 crystalline particle was smaller than undoped TiO_2 or Degussa P25 [65]. According to Yu et al. [133], doping TiO_2 with anionic S could be more difficult than with cationic ones given the different ionic radius of S^{2-} (1.7 Å), which is significantly larger than that of O^{2-} (1.22 Å). Consequently, Ti-S bonding requires larger formation energy than Ti-O bonding. Ti^{4+} is therefore replaced with S^{6+} as this union has chemical advantages over O^{2-} substitution by S^{2-}. As Fig. 4c explains, by substituting Ti^{4+} with S^{6+}, S_{3s} orbitals create states above the O_{2p} orbitals of TiO_2 valence band, and S_{3p} orbitals contribute to lowering TiO_2 conduction [131]. The ionic form of sulfur dopant depends on the preparation routes and sulfur source. For instance, the anionic form of S dopant was produced when TiS_2 was used as the source. In that case, S in TiS_2 was oxidized and the residual sulfur remains as S^{2-} [133].

(Figure 4)

(Table 5)

5.3. Co-doping TiO_2

Some researchers have focused on co-doping as one way to compensate for the drawbacks of single-doped TiO_2. This approach is explained in detail in the following sections. Various studies have performed TiO_2 co-doping by combining metal/non-metal and non-metal/non-metal dopants discussed below. However, few studies have considered metal/metal TiO_2 co-doping [108].

5.3.1. Metals co-doped

The physiochemical properties and doping mechanism of combining two different metals to co-dope TiO_2 have not been thoroughly investigated. Pham et al. [108] studied hexane and butyl acetate photodegradation on Ag/V co-doped TiO_2 deposited on polyurethane. According to their report, Ag^+ ions radius (1.26 Å) is much bigger than Ti^{4+} ions. In the case of V-doped TiO_2, due to the similar radii of V^{4+} (0.72 Å) and Ti^{4+} (0.74 Å) ions, vanadium was incorporated more easily into the TiO_2 lattice. V^{4+} ions could therefore substitute Ti^{4+} ions to form Ti-O-V bonds in

the TiO_2 lattice. Ag and V were incorporated into the co-doped TiO_2, which formed Ti^{3+}. Consequently, the Ti^{3+}/Ti^{4+} ratio of the Ag-V co-doped TiO_2 was higher than that of a single V or Ag-doped photocatalyst. This indicates that compared to single doping, Ag-V co-doped TiO_2 enhanced dopants incorporation, therefore increasing oxygen vacancies (or Ti^{3+} formation).

In other words, incorporating metal dopants produced oxygen vacancies in the TiO_2 lattice, reducing Ti^{4+} into Ti^{3+}. Moreover, the Ag and V co-doping TiO_2 could prevent the aggregation of Ag, Ag_2O, and V_2O_5, creating uniformly distributed particles on the surface of TiO_2 in the Ag-V co-doped TiO_2/PU photocatalysts. Additionally, in Ag and V co-doping TiO_2, vanadium increased the internal electron transfer in the TiO_2 lattice and silver enhanced internal electron transfer in the Ag_2O. Vanadium also improved exterior electron transfer between Ag_2O and TiO_2 [108]. Zhang et al. [134] reported that adding alkali metals ions (Li^+, Na^+, and K^+) to Pt/TiO_2 catalysts caused more atomically dispersed Pt species; improved the H_2O and O_2 activation efficiently; and promoted catalysts performance in HCHO oxidation. In another study on HCHO oxidation, Zhang et al. [135] found that Na addition also had a visible promoting effect on Pd/TiO_2 catalysts due to the good dispersion of Pd species.

5.3.2. Non-metals co-doped

Non-metals co-doped TiO_2 has been studied extensively [72, 120, 136]. The S-N co-doped TiO_2 exhibited strong absorption ability in both UV and visible light regions [10]. According to the XPS spectra of N, S and C tri-doped TiO_2 (NSC-TiO_2) in Lei et al. [136] research, N was assigned to the Ti-O-N and Ti-N bonds; S was mostly attributed to the Ti-O-S bond; and C was ascribed to the Ti-O-C bonds in the NSC-TiO_2 catalyst. In addition, results showed that co-doping and calcination temperature affects the catalyst microstructure and crystallite size. Li et al. [137] studied the degradation of gaseous acetaldehyde, toluene, and trichloroethylene in N and F-co-doped TiO_2 photocatalytic process. They found that co-doping nitrogen and fluorine has a synergetic effect. N doping enhanced visible light absorption, photocatalytic activity, and the formation of superoxide ($O_2^{\bullet -}$) radicals through the oxygen vacancies sites. F-doping formed new active sites and hydroxyl radicals ($OH^{\bullet}$).

Non-metals can be introduced into the TiO_2 lattice by applying various precursors and preparation methods (Table 3). In C and S co-doped or S-doped TiO_2, thiourea is generally used

as a non-metal doping source [72]. In the initial thermal treatment of catalyst preparation, thiourea was first decomposed by increasing the temperature. This temperature increase released N-containing gas, which can interact with Ti and O atoms to produce N dopants into the TiO_2 lattice. During the thermal treatment, many oxygen vacancies are produced and N-containing gas can easily enter the vacancies [72]. The formation of oxygen vacancies in N-doping TiO_2 happens because two nitrogen atoms should replace with three oxygen atoms to maintain electro neutrality, and so produce an oxygen vacancy in the TiO_2 crystal lattice. Furthermore, superoxide radicals ($O_2^{\bullet -}$) that require oxygen vacancy sites form [137].

5.3.3. Metal and non-metal co-doped

Dopant components in the TiO_2 lattice, including metal and non-metal, produce doping energy levels in the TiO_2 band gap that improve visible light absorption and result in higher photocatalytic performance (Fig. 5). Furthermore, metal components prefer to substitute for the Ti site in the TiO_2 lattice to create the dopant level near the conduction band. Non-metal components can potentially form new levels closest to the valence band that reduce the band gap and cause visible light absorption. Therefore, both metal and non-metal ion co-doping enhance photocatalytic activity [120, 138]. The synergistic effects between metal and non-metal dopants improve electron and hole separation, enhancing TiO_2 photocatalytic activity under visible light [120, 138].

(Figure 5)

It has also been reported that TiO_2 photoactivity when doped with nitrogen or sulfur can be improved by adding Fe(III) as a co-dopant [23]. N-Fe co-doped TiO_2 was studied by Dong et al. [120] in order to modify N-TiO_2 surface by Fe-ions. The results illustrated that a small amount of Fe-ions (0.02 wt.%) added to N-TiO_2 nanocrystal improved the catalyst photoactivity under visible and UV irradiation. It also improved augmented photodegradation efficiency to 97%. In addition, Fe-ions modification can also improve N-doped TiO_2 stability. In other words, N-doped photocatalyst instability by nitrogen loss happens when the photogenerated hole oxidizes the catalyst lattice nitrogen and gradually leads to deactivation. However, the lattice nitrogen was relatively stable due to Fe-ions surface modification in Fe/N-doped TiO_2 [120]. Li et al. [138] studied the C, Mo co-doped TiO_2 and reported that after Mo-doping TiO_2, the doping energy level was 0.4 eV. This level was extremely positive compared to the TiO_2 conduction band.

Consequently, the valence band electrons could be excited to the Mo^{6+}/Mo^{5+} doping energy level under visible irradiation. Li et al. [138] also argued that the recombination rate in C, Mo co-doped TiO_2 is lower than that of Mo-doped TiO_2.

Table 6 summarizes a number of co-doped TiO_2 photocatalysts synthesized to improve TiO_2 photocatalytic degradation performance. Different types of co-doped TiO_2 catalysts, including non-metal/non-metal, metal/metal, and metal/non-metal performance in the PCO of gas phase pollution and their operating parameters, are reviewed in Table 6.

(Table 6)

5.4. Composite semiconductors

One effective technique for improving TiO_2 photoactivity is coupling it with other semiconductors that generally have lower band gap energy. As a result, TiO_2 photoactivation expands to the visible region. Coupling catalysts are applied to accelerate electron and hole separation [36]. These semiconductors include WO_3 [106], SiO_2 [37], SnO_2 [21, 22, 55], $MnCO_3$ [139], CdS [140], Ag_3VO_4 [36], ZnO [141], and porous material with a large surface area (e.g. activated carbon) [10]. As illustrated in Table 7, semiconductors coupled with TiO_2 performed an enhanced photocatalytic degradation compared pure TiO_2. Different metal/non-metal doped with semiconductor composites are considered for improving TiO_2 photoactivity.

Among the different semiconductors reviewed, SnO_2 is interesting for having lattice parameters and a tetragonal structure similar to TiO_2. As Fig. 6a shows [21, 22, 142], in the TiO_2 and SnO_2 heterojunction, TiO_2 photogenerated electrons move to SnO_2 conduction band while holes transfer in the reverse direction, thereby separating charge carriers and suppressing recombination as a result [21, 22]. Substituting Sn (SnO_2) for Ti (TiO_2 lattice) can only cause a blue shift in TiO_2 light absorption spectra since SnO_2 band gap is larger than TiO_2. Consequently, to obtain visible light photoactivity, there should be a surface coupling between the two semiconductors [21].

Liu et al. [140] studied the degradation of benzene on CdS-TiO_2, which was supported on fiber glass cloth. TiO_2 and CdS can be excited under UV-vis irradiation to produce electron and hole pairs (Eq. 18). According to the electronic structure of mentioned semiconductor, the TiO_2

conduction band is more positive than that of CdS nanoparticles, which leads to the formation of a local electric field (Fig. 6b) [140, 142]. As a result, photogenerated electrons could transfer from CdS nanoparticles conduction band to the TiO_2, while the photogenerated holes in the TiO_2 semiconductors valence band accumulate in the CdS valence band to create a hole center (Eq. 19). Consequently, the recombination rate of charge carriers can be reduced effectively. For visible light illumination, only CdS nanoparticles can be excited and photogenerated electrons moved to the TiO_2 conduction band (Eqs. 20 and 21) [140].

$$CdS - TiO_2 \xrightarrow{UV-vis\ light} CdS(e^- + h^+) - TiO_2(e^- + h^+) \quad (18)$$

$$CdS(e^- + h^+) - TiO_2(e^- + h^+) \rightarrow CdS(h^+) - TiO_2(e^-) \quad (19)$$

$$CdS - TiO_2 \xrightarrow{Visible\ light} CdS(e^- + h^+) - TiO_2 \quad (20)$$

$$CdS(e^- + h^+) - TiO_2 \rightarrow CdS(h^+) - TiO_2(e^-) \quad (21)$$

Some studies have also focused on TiO_2/SiO_2 composite [37, 143-145]. Yu et al. [143] argued that in TiO_2/SiO_2 composite thin films, increasing SiO_2 percentages augments the surface hydroxyl. Consequently, the growth in surface hydroxyl content will trap more holes in the valence band and prevent charge carriers from recombining. In addition, TiO_2/SiO_2 photoactivity increased when SiO_2 was less than 5 mol% and decreased when higher than 10 mol%. Zou et al. [145] claimed that TiO_2/SiO_2 composite pellet shape had a higher adsorption capacity than thin film. Consequently, they acted as both photocatalyst and adsorbent. Zhan et al. [37] reported that in TiO_2/SiO_2 composites, increasing the doped silica molar ratio enhances the surface area of composite fibers. The larger surface area increases photocatalytic degradation efficiency. By contrast, the Ti–O–Si bond came out and resulted in lots of chemical defects on the surface of SiO_2 doped TiO_2 fibers, which can also enhance the oxidation rate. However, an excessive amount of high silica ratio recombines charge carriers and decreases the degradation rate [37].

Lee et al. [106] investigated the N-doped TiO_2/WO_3 composites photocatalytic degradation efficiency. The catalyst photoactivity enhanced with an increase in WO_3 loading from 0.5% to 4.0%. However, an additional increase in WO_3 loading to 6.0% reduced photocatalytic efficiency. Fig. 6c shows the electronic structure of composite WO_3-TiO_2, and demonstrates that electron and hole pairs could move between these semiconductors bands [106, 142].

As seen in Fig. 6d [146] and according to Ferrari-Lima et al. [105], the heterojunction of TiO_2 and ZnO semiconductors (which have similar a band gap), creates synergic effects, decreases the recombination rate, and increases charge carriers lifetime. For TiO_2-ZnO, the electron transfers

from ZnO conduction band to that of TiO_2, and the hole transfers from TiO_2 valence band to that of ZnO. As a result, the recombination rate of electron–hole pair decreases, and the charge carrier lifetime increases [105, 146, 147].

(Figure 6)

(Table 7)

6. Challenges

6.1. Limitation of doping

6.1.1. Limitations of metal doping

As pointed out earlier, metal doping TiO_2 impacts photocatalysis performance positively. However, earlier research has shown that doping TiO_2 with metal ions may have considerable drawbacks. Transition metals might cause partial blockage on TiO_2 porous surface sites [119] or cause the growth of particles. This would decrease the specific surface area and PCO performance subsequently [79]. As Table 4 and Yang et al. research [86] show, BTEX degradations on Fe-doped TiO_2 decreased under UV light because of a probable blockage, and therefore decreased in surface area. In addition, Korologos et al. [113] reported that benzene, toluene, and m-xylene degradation was not efficient in Fe/P25 and Pt/P25 under UV light irradiation.

Additionally, metal-doped TiO_2 catalysts have shown thermal instability [127, 128] and photo-corrosion [39]. Metal dopants may act as recombination centers, encouraging the recombination of photogenerated charge carriers [39, 87, 127]. When metal loading concentration is beyond optimum value, electron transfer from TiO_2 to metal dopants could deform the potential field in TiO_2 particles and charge metal centers negatively. This would draw a portion of holes near the metal—TiO_2 junction (especially for highly doped catalysts), and heighten the recombination rate. The deposited metal could also shield from photon absorption, which is detrimental to photocatalytic activity [148]. Sun et al. [73] reported that, for Fe-doped TiO_2, the separation and transportation efficiency of charge carriers enhanced when Fe^{3+} doping was increased from 0.1% to 0.7%, and significantly decreased when increased from 0.7% to 1.5%.

Moreover, although noble metals and rare earth metals could efficiently improve PCO, the cost-effectiveness required for industrial uses usually leads to more economical transitions or non-metals dopants being chosen.

6.1.2. Limitation of non-metal doping

Despite non-metal-doped TiO_2 photocatalytic performance with visible light, the photocatalyst presents some disadvantages. Doping non-metal dopants into the TiO_2 lattice causes oxygen vacancies to form in the bulk, which may become an important recombination center for charge carries. These defects limit visible light photocatalysis efficiency significantly [98]. The catalyst preparation method is one key parameter that should be considered for photocatalytic uses. Additionally, the doping procedure of non-metal dopants requires thermal treatment at high temperatures (400-850 ºC) or a long preparation time requiring high energy (see Table 3). Moreover, using toxic, expensive, or unstable precursors and the formation of undesirable gaseous by-products during the synthesizing process makes the preparation process costly and hinders large-scale production [38, 98]. Furthermore, the content of non-metal dopants would decrease during the annealing process and reduce visible-light photoactivity [149].

6.2. Stabilization by support structure

Catalyst immobilization is one key factor for heterogeneous PCO efficient removal of indoor air pollutants. Applying an effective coating method and substrate type, two critical parameters in catalyst immobilization, is important. Appropriate substrates should have stable physical and chemical properties in photochemical oxidation reactions. In addition, the substrate should provide a large surface area for the catalyst to coat on. Other essential properties of the substrate are: sufficient adhesion of the TiO_2 particles; resistance against sintering temperatures; and a strong absorbance affinity with contaminants. Different materials, such as activated carbon fibers [84], glass [65, 113], various polymeric materials [63, 108, 109], zeolites [150], fiberglass fiber [61, 81], carbon cloth fiber [61, 81], stainless steel [151], carbon nanotube [152], carbonized cotton fibers [59], and glass fibers (GFs) [86] have been used as support.

Glass and silica substrates are among the widest used materials because they are transparent. Activated carbon has high porosity, which creates a high specific surface area and enhances photocatalyst activity. Carbonized cotton fibers (CCFs) are an alternative support for TiO_2. CCFs

have great corrosion and temperature resistance, high conductivity, and strength. In addition, glass fibers (GFs) are flexible and easier to handle than other supports [59, 86].

Pham et al. [109] considered gaseous toluene degradation on V-doped TiO_2. Porous polyurethane (PU) was used as a support for immobilizing the photocatalyst and so increases its adsorption ability to remove toluene under visible light irradiation. In another study [63], they used PU as a substrate for Cu doped TiO_2 for benzene degradation. Immobilized on a porous support, Cu–TiO_2 showed improvement in both adsorption capacity and photocatalytic oxidation for benzene removal. Jo et al. [101] studied the aluminum sheet-based S-doped TiO_2 for BTEX photodegradation. Aluminum is considered a flexible low-cost substrate. Yang et al. [86] stated that stabilizing the nanocatalyst on the substrate in air purification system is essential. They considered BTEX photodegradation on Fe-doped TiO_2, which supported on the glass fiber. They examined the applicability of glass fiber supported photocatalyst for eliminating VOCs under visible and UV light irradiation. Zhong et al. [7] studied the photocatalytic oxidation process of TiO_2 coated on fiberglass fibers (FGFs) and carbon cloth fibers (CCFs). In this study, the photolysis effects under vacuum ultraviolet (VUV) and ultraviolet (UVC) irradiation for a different kind of VOCs were investigated in a pilot duct system. The single-pass removal efficiency of considered compounds showed the following sequence: TiO_2/CCFs+VUV > TiO_2/FGFs+VUV > TiO_2/FGFs+UVC. According to their results, coating nano-TiO_2 particles on the CCFs provided a large surface area that produced high photocatalytic activity. In a different study, Zhong et al. [61] reported that TiO_2 /FGFs catalyst possesses hydrophilic characteristics. Because of this, the adsorption coefficient for polar VOCs was higher than that of non-polar VOCs at the same RH level. Moreover, the BET surface area of TiO_2/CCFs being higher than that of TiO_2/FGFs led to a greater adsorption capacity [61].

A desirable coating technique should have the following requirements: a) a durable and stable coating; b) an efficient and appropriate contact between the catalyst and the contaminant; c) be non-selective for different substrates; and d) be cost-effective and suitable for large-scale application [153]. Generally, the dip coating and spray coating are used for immobilizing TiO_2 on the catalyst support [6, 40, 154]. Dip coating forms a thin and controllable layer, while spray coating may be used to create a thicker layer [59].

6.3. Application in industrial, civil and building construction

General studies considering the PCO for removal of a wide range of VOCs in the gas phase are reviewed in this paper. However, most reported studies are based on bench-scale operating in laboratory conditions and there are only a few papers dealing with full-scale or industrial application of PCO technology [7, 53, 61, 155, 156]. Although, the acceptable efficiency of PCO is proved in laboratory scales, there are some limitations during the scaling up the system which are operating in real conditions [157]. For example, the most reported research were done for a single compound with low airflow rate (in L/min level) and high VOCs concentration (in hundreds ppm level), which is far from real indoor applications [158]. Consequently, results from these research may not appropriately accurate and practical for the design of large-scale application of PCO for removal of VOCs [158].

Despite enormous studies on UV-PCO for removal of VOCs in the laboratory, limited research has been studied the catalyst deactivation problem, by-product production and moderate removal efficiency [158]. By-products and intermediates production and their accumulation on the surface of catalyst may cause the deactivation of catalyst [156, 159]. An additional concern that restricts full-scale applications of PCO in air purification system is their moderate efficiency, particularly when they are operating in high flow rate that is more similar to the real application [158]. Improvement of the catalyst surface characteristics in order to reduce the catalyst deactivation may address this limitation. The deactivation may be reduced through deferent strategies: a) expand the light absorption edge into the visible range that more photon could be used; b) reduce the recombination rate of charge carriers to enhance the quantum yield; c) design the PCO reactor with the configuration that the maximum light reach to the full surface of catalyst [158].

The large-scale applications of photocatalytic process were used for air purification and self-cleaning purposes for the first time in Japan, in middle of the 1990s [157]. One of the most successful self-cleaning coatings, which are used in the practical applications, is TiO_2-based photocatalytic coating. Many substrates such as window glass for building, concrete for construction and bridges, metal for traffic infrastructure and architecture, and polymers for

outdoor objects have been modified with TiO_2-based coating to achieve self-cleaning performance [160].

Zhong et al. [7] studied different VOCs removal in a pilot-scale application. They considered the operational parameters such as contaminant concentration, relative humidity, and residence time quite similar to the real conditions. They also reported the generated by-products for each compound. He et al. [156] studied the paint plant's waste gas removal in a pilot-scale system combined with PCO and biotrickling filtration (BTF). They reported that the combination of PCO and BTF is efficient for the removal of the high concentration and multicomponent VOCs from waste gas of paint plant.

7. Conclusion

PCO is a promising technology for air purification that can eliminate indoor air contaminants effectively at room temperature. PCO degrades hydrocarbon contaminants to carbon dioxide and water. However, in most cases, some hazardous by-products will inevitably form during PCO. Various factors such as humidity, light type and intensity, photocatalyst concentration, contaminant concentration, and flow rate can affect PCO efficiency.

TiO_2, the most used semiconductor photocatalysts in PCO, requires UV light irradiation to activate given its relatively wide band gap. As a result, visible light does not have sufficient energy to excite the electrons from the valence band to the TiO_2 conduction band. Doping TiO_2 with metal, non-metal and different composite semiconductors are promising methods for overcoming its inherent limitations and for enhancing photocatalytic activity under visible light irradiation. In addition, the effective reduction of electron and hole recombination rate is another result of doping.

Metal components create the dopant state near the conduction band, however, non-metal components form the new state closest to the valence band that lower the band gap and expand the TiO_2 light absorption edge. Moreover, the synergistic effects between metal and non-metal dopants in co-doped TiO_2 improve electron and hole separation, followed by enhancing TiO_2 photocatalytic activity under visible light. Coupling TiO_2 with other semiconductors that generally have lower band gap energy improves the TiO_2 photoactivity, accelerate electron and hole separation, and expands its light absorption to the visible region.

Furthermore, it is essential to find an optimum amount of dopant to increase the separation of charge carriers and prevent the formation of a recombination center. Additionally, choosing an appropriate synthesizing or coating method to improve the catalyst features should also be considered.

References

1. Yu, B.F., et al., *Review of research on air-conditioning systems and indoor air quality control for human health.* International Journal of Refrigeration, 2009. **32**(1): p. 3-20.
2. Cheng, Y.-H., C.-C. Lin, and S.-C. Hsu, *Comparison of conventional and green building materials in respect of VOC emissions and ozone impact on secondary carbonyl emissions.* Building and Environment, 2015. **87**: p. 274-282.
3. Guieysse, B., et al., *Biological treatment of indoor air for VOC removal: Potential and challenges.* Biotechnology Advances, 2008. **26**(5): p. 398-410.
4. Bahri, M. and F. Haghighat, *Plasma-Based Indoor Air Cleaning Technologies: The State of the Art-Review.* CLEAN – Soil, Air, Water, 2014. **42**(12): p. 1667-1680.
5. Zhang, G., et al., *Synthesis of bicrystalline TiO2 supported sepiolite fibers and their photocatalytic activity for degradation of gaseous formaldehyde.* Applied Clay Science, 2014. **102**: p. 231-237.
6. Yang, L., et al., *Design consideration of photocatalytic oxidation reactors using TiO2-coated foam nickels for degrading indoor gaseous formaldehyde.* Catalysis Today, 2007. **126**(3–4): p. 359-368.
7. Zhong, L., et al., *Performance of ultraviolet photocatalytic oxidation for indoor air applications: Systematic experimental evaluation.* Journal of Hazardous Materials, 2013. **261**: p. 130-138.
8. Farhanian, D. and F. Haghighat, *Photocatalytic oxidation air cleaner: Identification and quantification of by-products.* Building and Environment, 2014. **72**: p. 34-43.
9. Gaya, U.I. and A.H. Abdullah, *Heterogeneous photocatalytic degradation of organic contaminants over titanium dioxide: A review of fundamentals, progress and problems.* Journal of Photochemistry and Photobiology C: Photochemistry Reviews, 2008. **9**(1): p. 1-12.
10. Tseng, T.K., et al., *A Review of Photocatalysts Prepared by Sol-Gel Method for VOCs Removal.* International Journal of Molecular Sciences, 2010. **11**(6): p. 2336.
11. Ji, J., et al., *Mesoporous TiO2 under VUV irradiation: Enhanced photocatalytic oxidation for VOCs degradation at room temperature.* Chemical Engineering Journal, 2017. **327**(Supplement C): p. 490-499.
12. Tejasvi, R., M. Sharma, and K. Upadhyay, *Passive photo-catalytic destruction of air-borne VOCs in high traffic areas using TiO2-coated flexible PVC sheet.* Chemical Engineering Journal, 2015. **262**(Supplement C): p. 875-881.
13. Lopes, F.V.S., et al., *Insights into UV-TiO2 photocatalytic degradation of PCE for air decontamination systems.* Chemical Engineering Journal, 2012. **204**(Supplement C): p. 244-257.

14. Galliano, S., et al., *Photoanode/Electrolyte Interface Stability in Aqueous Dye-Sensitized Solar Cells.* Energy Technology, 2017. **5**(2): p. 300-311.
15. Bella, F., et al., *Unveiling the controversial mechanism of reversible Na storage in TiO2 nanotube arrays: Amorphous versus anatase TiO2.* Nano Research, 2017. **10**(8): p. 2891-2903.
16. Bella, F., et al., *Paper-based quasi-solid dye-sensitized solar cells.* Electrochimica Acta, 2017. **237**(Supplement C): p. 87-93.
17. Hou, X., et al., *Efficient quasi-mesoscopic perovskite solar cells using Li-doped hierarchical TiO2 as scaffold of scattered distribution.* Chemical Engineering Journal, 2017. **330**(Supplement C): p. 947-955.
18. Yu, J., et al., *Enhancement of Photocatalytic Activity of Mesporous TiO2 Powders by Hydrothermal Surface Fluorination Treatment.* The Journal of Physical Chemistry C, 2009. **113**(16): p. 6743-6750.
19. Zeng, L., et al., *A modular calcination method to prepare modified N-doped TiO2 nanoparticle with high photocatalytic activity.* Applied Catalysis B: Environmental, 2016. **183**: p. 308-316.
20. Feng, Y., et al., *Improved Catalytic Capability of Mesoporous TiO2 Microspheres and Photodecomposition of Toluene.* ACS Applied Materials & Interfaces, 2010. **2**(11): p. 3134-3140.
21. Khan, R. and T.-J. Kim, *Preparation and application of visible-light-responsive Ni-doped and SnO2-coupled TiO2 nanocomposite photocatalysts.* Journal of Hazardous Materials, 2009. **163**(2–3): p. 1179-1184.
22. Zhao, W., et al., *Synthesis, Characterization, and Photocatalytic Properties of SnO2/Rutile TiO2/Anatase TiO2 Heterojunctions Modified by Pt.* The Journal of Physical Chemistry C, 2014. **118**(40): p. 23117-23125.
23. Khan, R., et al., *Comparative study of the photocatalytic performance of boron–iron Co-doped and boron-doped TiO2 nanoparticles.* Materials Chemistry and Physics, 2008. **112**(1): p. 167-172.
24. Bianchi, C.L., et al., *N-doped TiO2 from TiCl3 for photodegradation of air pollutants.* Catalysis Today, 2009. **144**(1–2): p. 31-36.
25. Ferrari-Lima, A.M., et al., *Synthesis, characterisation and photocatalytic activity of N-doped TiO2–Nb2O5 mixed oxides.* Catalysis Today, 2015. **254**: p. 119-128.
26. Burns, A., et al., *Neodymium ion dopant effects on the phase transformation in sol–gel derived titania nanostructures.* Materials Science and Engineering: B, 2004. **111**(2–3): p. 150-155.
27. Chen, H., C.E. Nanayakkara, and V.H. Grassian, *Titanium Dioxide Photocatalysis in Atmospheric Chemistry.* Chemical Reviews, 2012. **112**(11): p. 5919-5948.
28. Dhada, I., P.K. Nagar, and M. Sharma, *Challenges of TiO2-Based Photooxidation of Volatile Organic Compounds: Designing, Coating, and Regenerating Catalyst.* Industrial & Engineering Chemistry Research, 2015. **54**(20): p. 5381-5387.
29. Sarkar, D., et al., *Three Dimensional Ag2O/TiO2 Type-II (p–n) Nanoheterojunctions for Superior Photocatalytic Activity.* ACS Applied Materials & Interfaces, 2013. **5**(2): p. 331-337.
30. Vildozo, D., et al., *Photocatalytic treatment of indoor air: Optimization of 2-propanol removal using a response surface methodology (RSM).* Applied Catalysis B: Environmental, 2010. **94**(3–4): p. 303-310.

31. Guo, L., Y. Wang, and H.P. Lu, *Combined Single-Molecule Photon-Stamping Spectroscopy and Femtosecond Transient Absorption Spectroscopy Studies of Interfacial Electron Transfer Dynamics.* Journal of the American Chemical Society, 2010. **132**(6): p. 1999-2004.
32. Yamada, Y. and Y. Kanemitsu, *Determination of electron and hole lifetimes of rutile and anatase TiO2 single crystals.* Applied Physics Letters, 2012. **101**(13): p. 133907.
33. Ozawa, K., et al., *Electron–Hole Recombination Time at TiO2 Single-Crystal Surfaces: Influence of Surface Band Bending.* The Journal of Physical Chemistry Letters, 2014. **5**(11): p. 1953-1957.
34. Lee, M.H., E. Geva, and B.D. Dunietz, *Calculation from First-Principles of Golden Rule Rate Constants for Photoinduced Subphthalocyanine/Fullerene Interfacial Charge Transfer and Recombination in Organic Photovoltaic Cells.* The Journal of Physical Chemistry C, 2014. **118**(18): p. 9780-9789.
35. Mohtasebi, A., et al., *Interfacial Charge Transfer between Phenyl-Capped Aniline Tetramer Films and Iron Oxide Surfaces.* The Journal of Physical Chemistry C, 2016. **120**(51): p. 29248-29263.
36. Wang, J., et al., *Highly Efficient Oxidation of Gaseous Benzene on Novel Ag3VO4/TiO2 Nanocomposite Photocatalysts under Visible and Simulated Solar Light Irradiation.* The Journal of Physical Chemistry C, 2012. **116**(26): p. 13935-13943.
37. Zhan, S., et al., *Rapid degradation of toxic toluene using novel mesoporous SiO2 doped TiO2 nanofibers.* Catalysis Today, 2014. **225**: p. 10-17.
38. Dong, F., H. Wang, and Z. Wu, *One-Step "Green" Synthetic Approach for Mesoporous C-Doped Titanium Dioxide with Efficient Visible Light Photocatalytic Activity.* The Journal of Physical Chemistry C, 2009. **113**(38): p. 16717-16723.
39. Jo, W.-K. and J.-T. Kim, *Application of visible-light photocatalysis with nitrogen-doped or unmodified titanium dioxide for control of indoor-level volatile organic compounds.* Journal of Hazardous Materials, 2009. **164**(1): p. 360-366.
40. Han, Z., et al., *Experimental study on visible-light induced photocatalytic oxidation of gaseous formaldehyde by polyester fiber supported photocatalysts.* Chemical Engineering Journal, 2013. **218**: p. 9-18.
41. Hussain, M., N. Russo, and G. Saracco, *Photocatalytic abatement of VOCs by novel optimized TiO2 nanoparticles.* Chemical Engineering Journal, 2011. **166**(1): p. 138-149.
42. Le Bechec, M., et al., *Comparison of kinetics of acetone, heptane and toluene photocatalytic mineralization over TiO2 microfibers and Quartzel® mats.* Applied Catalysis B: Environmental, 2015. **179**: p. 78-87.
43. Hussain, M., et al., *Synthesis, characterization, and photocatalytic application of novel TiO2 nanoparticles.* Chemical Engineering Journal, 2010. **157**(1): p. 45-51.
44. Agatino Di Paola , Marianna Bellardita, and a.L. Palmisano, *Brookite, the Least Known TiO2 Photocatalyst.* catalysts, 2013: p. 36-73.
45. Guimaraes, R.R., A.L.A. Parussulo, and K. Araki, *Impact of nanoparticles preparation method on the synergic effect in anatase/rutile mixtures.* Electrochimica Acta, 2016. **222**(Supplement C): p. 1378-1386.
46. Verbruggen, S.W., *TiO2 photocatalysis for the degradation of pollutants in gas phase: From morphological design to plasmonic enhancement.* Journal of Photochemistry and Photobiology C: Photochemistry Reviews, 2015. **24**: p. 64-82.
47. Pfeifer, V., et al., *Energy Band Alignment between Anatase and Rutile TiO2.* The Journal of Physical Chemistry Letters, 2013. **4**(23): p. 4182-4187.

48. Wang, C. and T. Wu, *TiO2 nanoparticles with efficient photocatalytic activity towards gaseous benzene degradation.* Ceramics International, 2015. **41**(2, Part B): p. 2836-2839.
49. Bianchi, C.L., et al., *Photocatalytic degradation of acetone, acetaldehyde and toluene in gas-phase: Comparison between nano and micro-sized TiO2.* Applied Catalysis B: Environmental, 2014. **146**: p. 123-130.
50. Nakata, K. and A. Fujishima, *TiO2 photocatalysis: Design and applications.* Journal of Photochemistry and Photobiology C: Photochemistry Reviews, 2012. **13**(3): p. 169-189.
51. Sun, Q., et al., *Influence of calcination temperature on the structural, adsorption and photocatalytic properties of TiO2 nanoparticles supported on natural zeolite.* Powder Technology, 2015. **274**: p. 88-97.
52. Aghighi, A. and F. Haghighat, *Using physical–chemical properties of reactants to estimate the performance of photocatalytic oxidation air cleaners.* Building and Environment, 2015. **85**: p. 114-122.
53. Farhanian, D., et al., *Impact of design parameters on the performance of ultraviolet photocatalytic oxidation air cleaner.* Building and Environment, 2013. **66**(Supplement C): p. 148-157.
54. Mamaghani, A.H., F. Haghighat, and C.-S. Lee, *Photocatalytic oxidation technology for indoor environment air purification: The state-of-the-art.* Applied Catalysis B: Environmental, 2017. **203**: p. 247-269.
55. Fresno, F., et al., *Photocatalytic degradation of toluene over doped and coupled (Ti,M)O2 (M = Sn or Zr) nanocrystalline oxides: Influence of the heteroatom distribution on deactivation.* Applied Catalysis B: Environmental, 2008. **84**(3–4): p. 598-606.
56. Korologos, C.A., C.J. Philippopoulos, and S.G. Poulopoulos, *The effect of water presence on the photocatalytic oxidation of benzene, toluene, ethylbenzene and m-xylene in the gas-phase.* Atmospheric Environment, 2011. **45**(39): p. 7089-7095.
57. Sharmin, R. and M.B. Ray, *Application of ultraviolet light-emitting diode photocatalysis to remove volatile organic compounds from indoor air.* Journal of the Air & Waste Management Association, 2012. **62**(9): p. 1032-1039.
58. Takeuchi, M., et al., *Effect of H2O vapor addition on the photocatalytic oxidation of ethanol, acetaldehyde and acetic acid in the gas phase on TiO2 semiconductor powders.* Applied Catalysis B: Environmental, 2010. **96**(1–2): p. 218-223.
59. Wang, B., et al., *High photocatalytic activity of immobilized TiO2 nanorods on carbonized cotton fibers.* Journal of Hazardous Materials, 2013. **263, Part 2**: p. 659-669.
60. Muñoz-Batista, M.J., et al., *Sunlight-driven toluene photo-elimination using CeO2-TiO2 composite systems: A kinetic study.* Applied Catalysis B: Environmental, 2013. **140–141**: p. 626-635.
61. Zhong, L., C.-S. Lee, and F. Haghighat, *Adsorption performance of titanium dioxide (TiO2) coated air filters for volatile organic compounds.* Journal of Hazardous Materials, 2012. **243**: p. 340-349.
62. Wu, Y.-T., et al., *Enhanced xylene removal by photocatalytic oxidation using fiber-illuminated honeycomb reactor at ppb level.* Journal of Hazardous Materials, 2013. **262**: p. 717-725.
63. Pham, T.-D., B.-K. Lee, and C.-H. Lee, *The advanced removal of benzene from aerosols by photocatalytic oxidation and adsorption of Cu–TiO2/PU under visible light irradiation.* Applied Catalysis B: Environmental, 2016. **182**: p. 172-183.

64. Tseng, H.-H., et al., *Degradation of xylene vapor over Ni-doped TiO2 photocatalysts prepared by polyol-mediated synthesis.* Chemical Engineering Journal, 2009. **150**(1): p. 160-167.
65. Jo, W.-K. and J.-T. Kim, *Decomposition of gas-phase aromatic hydrocarbons by applying an annular-type reactor coated with sulfur-doped photocatalyst under visible-light irradiation.* Journal of Chemical Technology & Biotechnology, 2010. **85**(4): p. 485-492.
66. Han, Z., et al., *Experimental study on visible-light induced photocatalytic oxidation of gaseous formaldehyde by polyester fiber supported photocatalysts.* Chemical Engineering Journal, 2013. **218**(Supplement C): p. 9-18.
67. Yang, L., et al., *Degradation of indoor gaseous formaldehyde by hybrid VUV and TiO2/UV processes.* Separation and Purification Technology, 2007. **54**(2): p. 204-211.
68. da Costa Filho, B.M., et al., *Intensification of heterogeneous TiO2 photocatalysis using an innovative micro-meso-structured-photoreactor for n-decane oxidation at gas phase.* Chemical Engineering Journal, 2017. **310**(Part 2): p. 331-341.
69. Zhu, X., et al., *Inherent rate constants and humidity impact factors of anatase TiO2 film in photocatalytic removal of formaldehyde from air.* Chemical Engineering Journal, 2015. **279**: p. 897-903.
70. El-Roz, M., et al., *New Operando IR Technique to Study the Photocatalytic Activity and Selectivity of TiO2 Nanotubes in Air Purification: Influence of Temperature, UV Intensity, and VOC Concentration.* The Journal of Physical Chemistry C, 2012. **116**(24): p. 13252-13263.
71. Daghrir, R., P. Drogui, and D. Robert, *Modified TiO2 For Environmental Photocatalytic Applications: A Review.* Industrial & Engineering Chemistry Research, 2013. **52**(10): p. 3581-3599.
72. Fan, D., Z. Weirong, and W. Zhongbiao, *Characterization and photocatalytic activities of C, N and S co-doped TiO 2 with 1D nanostructure prepared by the nano-confinement effect.* Nanotechnology, 2008. **19**(36): p. 365607.
73. Sun, S., et al., *Photocatalytic degradation of gaseous toluene on Fe-TiO2 under visible light irradiation: A study on the structure, activity and deactivation mechanism.* Applied Surface Science, 2012. **258**(12): p. 5031-5037.
74. Pinho, L., M. Rojas, and M.J. Mosquera, *Ag–SiO2–TiO2 nanocomposite coatings with enhanced photoactivity for self-cleaning application on building materials.* Applied Catalysis B: Environmental, 2015. **178**: p. 144-154.
75. Liu, B. and X. Zhao, *A kinetic model for evaluating the dependence of the quantum yield of nano-TiO2 based photocatalysis on light intensity, grain size, carrier lifetime, and minority carrier diffusion coefficient: Indirect interfacial charge transfer.* Electrochimica Acta, 2010. **55**(12): p. 4062-4070.
76. Salvadó-Estivill, I., D.M. Hargreaves, and G. Li Puma, *Evaluation of the Intrinsic Photocatalytic Oxidation Kinetics of Indoor Air Pollutants.* Environmental Science & Technology, 2007. **41**(6): p. 2028-2035.
77. Huang, H., et al., *Photocatalytic Oxidation of Gaseous Benzene under VUV Irradiation over TiO2/Zeolites Catalysts.* Catalysis Today, 2017. **281, Part 3**: p. 649-655.
78. Huang, H., et al., *Photocatalytic destruction of air pollutants with vacuum ultraviolet (VUV) irradiation.* Catalysis Today, 2011. **175**(1): p. 310-315.

79. Huang, H., et al., *Enhanced degradation of gaseous benzene under vacuum ultraviolet (VUV) irradiation over TiO2 modified by transition metals.* Chemical Engineering Journal, 2015. **259**: p. 534-541.
80. Huang, H. and W. Li, *Destruction of toluene by ozone-enhanced photocatalysis: Performance and mechanism.* Applied Catalysis B: Environmental, 2011. **102**(3–4): p. 449-453.
81. Zhong, L., F. Haghighat, and C.-S. Lee, *Ultraviolet photocatalytic oxidation for indoor environment applications: Experimental validation of the model.* Building and Environment, 2013. **62**: p. 155-166.
82. Moulis, F. and J. Krýsa, *Photocatalytic degradation of several VOCs (n-hexane, n-butyl acetate and toluene) on TiO2 layer in a closed-loop reactor.* Catalysis Today, 2013. **209**: p. 153-158.
83. Abbas, N., et al., *Studies on the activity and deactivation of novel optimized TiO2 nanoparticles for the abatement of VOCs.* Chemical Engineering Journal, 2011. **175**: p. 330-340.
84. Guo, T., et al., *Influence of relative humidity on the photocatalytic oxidation (PCO) of toluene by TiO2 loaded on activated carbon fibers: PCO rate and intermediates accumulation.* Applied Catalysis B: Environmental, 2008. **79**(2): p. 171-178.
85. Boulamanti, A.K., C.A. Korologos, and C.J. Philippopoulos, *The rate of photocatalytic oxidation of aromatic volatile organic compounds in the gas-phase.* Atmospheric Environment, 2008. **42**(34): p. 7844-7850.
86. Yang, S.-B., et al., *Iron-functionalized titanium dioxide on flexible glass fibers for photocatalysis of benzene, toluene, ethylbenzene, and o-xylene (BTEX) under visible- or ultraviolet-light irradiation.* Journal of the Air & Waste Management Association, 2015. **65**(3): p. 365-373.
87. Christoforidis, K.C., S.J.A. Figueroa, and M. Fernández-García, *Iron–sulfur codoped TiO2 anatase nano-materials: UV and sunlight activity for toluene degradation.* Applied Catalysis B: Environmental, 2012. **117–118**: p. 310-316.
88. Albrbar, A.J., et al., *Visible-light active mesoporous, nanocrystalline N,S-doped and co-doped titania photocatalysts synthesized by non-hydrolytic sol-gel route.* Ceramics International, 2016. **42**(15): p. 16718-16728.
89. Chu, S.-Z., et al., *Fabrication and Photocatalytic Characterizations of Ordered Nanoporous X-Doped (X = N, C, S, Ru, Te, and Si) TiO2/Al2O3 Films on ITO/Glass.* Langmuir, 2005. **21**(17): p. 8035-8041.
90. Tieng, S., A. Kanaev, and K. Chhor, *New homogeneously doped Fe(III)–TiO2 photocatalyst for gaseous pollutant degradation.* Applied Catalysis A: General, 2011. **399**(1–2): p. 191-197.
91. Murcia, J.J., et al., *Ethanol partial photoxidation on Pt/TiO2 catalysts as green route for acetaldehyde synthesis.* Catalysis Today, 2012. **196**(1): p. 101-109.
92. Barakat, T., et al., *Total oxidation of toluene over noble metal based Ce, Fe and Ni doped titanium oxides.* Applied Catalysis B: Environmental, 2014. **146**: p. 138-146.
93. Huang, H. and D.Y.C. Leung, *Complete elimination of indoor formaldehyde over supported Pt catalysts with extremely low Pt content at ambient temperature.* Journal of Catalysis, 2011. **280**(1): p. 60-67.
94. Murcia, J.J., et al., *Cyclohexane photocatalytic oxidation on Pt/TiO2 catalysts.* Catalysis Today, 2013. **209**: p. 164-169.

95. Houšková, V., et al., *Efficient gas phase photodecomposition of acetone by Ru-doped Titania.* Applied Catalysis B: Environmental, 2009. **89**(3–4): p. 613-619.
96. Menéndez-Flores, V.M. and T. Ohno, *High visible-light active Ir-doped-TiO2 brookite photocatalyst synthesized by hydrothermal microwave-assisted process.* Catalysis Today, 2014. **230**: p. 214-220.
97. Kim, M.-S., et al., *Preparation of porous carbon-doped TiO2 film by sol–gel method and its application for the removal of gaseous toluene in the optical fiber reactor.* Journal of Industrial and Engineering Chemistry, 2011. **17**(2): p. 223-228.
98. Dong, F., et al., *Enhancement of the Visible Light Photocatalytic Activity of C-Doped TiO2 Nanomaterials Prepared by a Green Synthetic Approach.* The Journal of Physical Chemistry C, 2011. **115**(27): p. 13285-13292.
99. Wang, H., Z. Wu, and Y. Liu, *A Simple Two-Step Template Approach for Preparing Carbon-Doped Mesoporous TiO2 Hollow Microspheres.* The Journal of Physical Chemistry C, 2009. **113**(30): p. 13317-13324.
100. Khalilzadeh, A. and S. Fatemi, *Spouted bed reactor for VOC removal by modified nano-TiO2 photocatalytic particles.* Chemical Engineering Research and Design, 2016. **115, Part A**: p. 241-250.
101. Jo, W.-K. and H.-J. Kang, *Aluminum sheet-based S-doped TiO2 for photocatalytic decomposition of toxic organic vapors.* Chinese Journal of Catalysis, 2014. **35**(7): p. 1189-1195.
102. Nishijima, K., et al., *Development of an S-doped titania nanotube (TNT) site-selectively loaded with iron(III) oxide and its photocatalytic activities.* Applied Catalysis B: Environmental, 2008. **84**(3–4): p. 584-590.
103. Li, Y., C. Zhang, and H. He, *Significant enhancement in activity of Pd/TiO2 catalyst for formaldehyde oxidation by Na addition.* Catalysis Today, 2017. **281, Part 3**: p. 412-417.
104. Zhou, M. and J. Yu, *Preparation and enhanced daylight-induced photocatalytic activity of C,N,S-tridoped titanium dioxide powders.* Journal of Hazardous Materials, 2008. **152**(3): p. 1229-1236.
105. Ferrari-Lima, A.M., et al., *Photodegradation of benzene, toluene and xylenes under visible light applying N-doped mixed TiO2 and ZnO catalysts.* Catalysis Today, 2015. **241, Part A**: p. 40-46.
106. Lee, J.Y. and W.-K. Jo, *Heterojunction-based two-dimensional N-doped TiO2/WO3 composite architectures for photocatalytic treatment of hazardous organic vapor.* Journal of Hazardous Materials, 2016. **314**: p. 22-31.
107. Vargas Hernández, J., et al., *Effects of metal doping (Cu, Ag, Eu) on the electronic and optical behavior of nanostructured TiO2.* Journal of Alloys and Compounds, 2017. **710**: p. 355-363.
108. Pham, T.-D. and B.-K. Lee, *Selective removal of polar VOCs by novel photocatalytic activity of metals co-doped TiO2/PU under visible light.* Chemical Engineering Journal, 2017. **307**: p. 63-73.
109. Pham, T.-D. and B.-K. Lee, *Novel adsorption and photocatalytic oxidation for removal of gaseous toluene by V-doped TiO2/PU under visible light.* Journal of Hazardous Materials, 2015. **300**: p. 493-503.
110. Stucchi, M., et al., *Copper NPs decorated titania: A novel synthesis by high energy US with a study of the photocatalytic activity under visible light.* Ultrasonics Sonochemistry, 2016. **31**: p. 295-301.

111. Choi, J., H. Park, and M.R. Hoffmann, *Effects of Single Metal-Ion Doping on the Visible-Light Photoreactivity of TiO2.* The Journal of Physical Chemistry C, 2010. **114**(2): p. 783-792.
112. Shao, G.N., et al., *Investigation of the influence of vanadium, iron and nickel dopants on the morphology, and crystal structure and photocatalytic properties of titanium dioxide based nanopowders.* Journal of Colloid and Interface Science, 2016. **474**: p. 179-189.
113. Korologos, C.A., et al., *Photocatalytic oxidation of benzene, toluene, ethylbenzene and m-xylene in the gas-phase over TiO2-based catalysts.* Journal of Photochemistry and Photobiology A: Chemistry, 2012. **244**: p. 24-31.
114. Li, X., et al., *Photocatalytic degradation of gaseous toluene over Ag-doping TiO2 nanotube powder prepared by anodization coupled with impregnation method.* Chemosphere, 2011. **83**(5): p. 674-679.
115. Mogal, S.I., et al., *Single-Step Synthesis of Silver-Doped Titanium Dioxide: Influence of Silver on Structural, Textural, and Photocatalytic Properties.* Industrial & Engineering Chemistry Research, 2014. **53**(14): p. 5749-5758.
116. Cheng, Z., et al., *Synthesis, characterization, and photocatalytic activity of porous La–N–co-doped TiO2 nanotubes for gaseous chlorobenzene oxidation.* Journal of Environmental Sciences, 2016. **46**(Supplement C): p. 203-213.
117. Yurtsever, H.A. and M. Çiftçioğlu, *The effect of rare earth element doping on the microstructural evolution of sol-gel titania powders.* Journal of Alloys and Compounds, 2017. **695**: p. 1336-1353.
118. Li, F.B., et al., *Enhanced photocatalytic degradation of VOCs using Ln3+–TiO2 catalysts for indoor air purification.* Chemosphere, 2005. **59**(6): p. 787-800.
119. Xiao, J., et al., *Preparation, phase transformation and photocatalytic activities of cerium-doped mesoporous titania nanoparticles.* Journal of Solid State Chemistry, 2006. **179**(4): p. 1161-1170.
120. Dong, F., et al., *Marked enhancement of photocatalytic activity and photochemical stability of N–doped TiO2 nanocrystals by Fe3+/Fe2+ surface modification.* Journal of Colloid and Interface Science, 2010. **343**(1): p. 200-208.
121. Hung, W.-C., et al., *Synthesis and characterization of TiO2 and Fe/TiO2 nanoparticles and their performance for photocatalytic degradation of 1,2-dichloroethane.* Applied Surface Science, 2008. **255**(5, Part 1): p. 2205-2213.
122. Chun, H.-H., J.Y. Lee, and W.-K. Jo, *Photocatalysis of low-concentration gaseous organic pollutants over electrospun iron-doped titanium dioxide nanofibers.* Solid State Sciences, 2013. **25**: p. 103-109.
123. Yu, H., et al., *Photocatalytic activity of TiO2 thin film non-uniformly doped by Ni.* Materials Chemistry and Physics, 2006. **97**(1): p. 59-63.
124. Tobaldi, D.M., et al., *Visible light activated photocatalytic behaviour of rare earth modified commercial TiO2.* Materials Research Bulletin, 2014. **50**: p. 183-190.
125. Inturi, S.N.R., et al., *Visible-light-induced photodegradation of gas phase acetonitrile using aerosol-made transition metal (V, Cr, Fe, Co, Mn, Mo, Ni, Cu, Y, Ce, and Zr) doped TiO2.* Applied Catalysis B: Environmental, 2014. **144**: p. 333-342.
126. Chen, D., et al., *Carbon and Nitrogen Co-doped TiO2 with Enhanced Visible-Light Photocatalytic Activity.* Industrial & Engineering Chemistry Research, 2007. **46**(9): p. 2741-2746.
127. Burda, C., et al., *Enhanced Nitrogen Doping in TiO2 Nanoparticles.* Nano Letters, 2003. **3**(8): p. 1049-1051.

128. Pandian, R., et al., *Types of nitrogen incorporation in reactively sputtered titania thin films: Influence on UV–visible, photocatalytic and photoconduction properties.* Thin Solid Films, 2016. **616**: p. 466-476.
129. Di Valentin, C., G. Pacchioni, and A. Selloni, *Theory of Carbon Doping of Titanium Dioxide.* Chemistry of Materials, 2005. **17**(26): p. 6656-6665.
130. Kavitha, R. and L.G. Devi, *Synergistic effect between carbon dopant in titania lattice and surface carbonaceous species for enhancing the visible light photocatalysis.* Journal of Environmental Chemical Engineering, 2014. **2**(2): p. 857-867.
131. Ma, D., et al., *Fabrication and photocatalytic properties of cationic and anionic S-doped TiO2 nanofibers by electrospinning.* Applied Catalysis B: Environmental, 2014. **147**: p. 49-57.
132. Ohno, T., et al., *Preparation of S-doped TiO2 photocatalysts and their photocatalytic activities under visible light.* Applied Catalysis A: General, 2004. **265**(1): p. 115-121.
133. Yu, J.C., et al., *Efficient Visible-Light-Induced Photocatalytic Disinfection on Sulfur-Doped Nanocrystalline Titania.* Environmental Science & Technology, 2005. **39**(4): p. 1175-1179.
134. Zhang, C., et al., *Alkali-Metal-Promoted Pt/TiO2 Opens a More Efficient Pathway to Formaldehyde Oxidation at Ambient Temperatures.* Angewandte Chemie International Edition, 2012. **51**(38): p. 9628-9632.
135. Zhang, C., et al., *Sodium-Promoted Pd/TiO2 for Catalytic Oxidation of Formaldehyde at Ambient Temperature.* Environmental Science & Technology, 2014. **48**(10): p. 5816-5822.
136. Lei, X.F., et al., *Effect of calcination temperature on the structure and visible-light photocatalytic activities of (N, S and C) co-doped TiO2 nano-materials.* Applied Surface Science, 2015. **332**: p. 172-180.
137. Li, D., et al., *Visible-light-driven nitrogen-doped TiO2 photocatalysts: effect of nitrogen precursors on their photocatalysis for decomposition of gas-phase organic pollutants.* Materials Science and Engineering: B, 2005. **117**(1): p. 67-75.
138. Li, Y.-F., et al., *Mechanistic Study of Codoped Titania with Nonmetal and Metal Ions: A Case of C + Mo Codoped TiO2.* ACS Catalysis, 2012. **2**(3): p. 391-398.
139. Feng, C., et al., *Visible light photocatalytic behavior of manganese carbonate/titanium dioxide nanocomposites based on photoinduced interfacial charge transfer.* Materials Letters, 2015. **155**: p. 23-26.
140. Liu, Z., et al., *Photocatalytic degradation of gaseous benzene with CdS-sensitized TiO2 film coated on fiberglass cloth.* Journal of Molecular Catalysis A: Chemical, 2012. **363–364**: p. 159-165.
141. Gholami, M., et al., *Comparison of Benzene & Toluene removal from synthetic polluted air with use of Nano photocatalyticTiO2/ ZNO process.* Journal of Environmental Health Science and Engineering, 2014. **12**(1): p. 45.
142. Xu, Y. and M.A.A. Schoonen, *The absolute energy positions of conduction and valence bands of selected semiconducting minerals.* American Mineralogist, 2000. **85**(3-4): p. 543-556.
143. Yu, J., J.C. Yu, and X. Zhao, *The Effect of SiO2 Addition on the Grain Size and Photocatalytic Activity of TiO2 Thin Films.* Journal of Sol-Gel Science and Technology, 2002. **24**(2): p. 95-103.
144. Guan, K., *Relationship between photocatalytic activity, hydrophilicity and self-cleaning effect of TiO2/SiO2 films.* Surface and Coatings Technology, 2005. **191**(2–3): p. 155-160.

145. Zou, L., et al., *Removal of VOCs by photocatalysis process using adsorption enhanced TiO2–SiO2 catalyst.* Chemical Engineering and Processing: Process Intensification, 2006. **45**(11): p. 959-964.
146. Li, X., J. Yu, and M. Jaroniec, *Hierarchical photocatalysts.* Chemical Society Reviews, 2016. **45**(9): p. 2603-2636.
147. Liu, R., et al., *Fabrication of TiO2/ZnO composite nanofibers by electrospinning and their photocatalytic property.* Materials Chemistry and Physics, 2010. **121**(3): p. 432-439.
148. Gomathi Devi, L. and R. Kavitha, *A review on plasmonic metal□TiO2 composite for generation, trapping, storing and dynamic vectorial transfer of photogenerated electrons across the Schottky junction in a photocatalytic system.* Applied Surface Science, 2016. **360, Part B**: p. 601-622.
149. Chen, Q., et al., *Visible-light-activated Ce–Si co-doped TiO2 photocatalyst.* Applied Surface Science, 2009. **255**(18): p. 7918-7924.
150. Yuan, J., et al., *Ozone-assisted photocatalytic degradation of gaseous acetaldehyde on TiO2/M-ZSM-5 (M = Zn, Cu, Mn).* Catalysis Today, 2013. **201**: p. 182-188.
151. Cao, S., et al., *Highly antibacterial activity of N-doped TiO2 thin films coated on stainless steel brackets under visible light irradiation.* Applied Surface Science, 2014. **309**: p. 119-127.
152. Daram, P., et al., *Microstructure and photocatalytic activities of thermal sprayed titanium dioxide/carbon nanotubes composite coatings.* Surface and Coatings Technology, 2016. **306, Part A**: p. 290-294.
153. Han, Z., et al., *Preparation of TiO2-Coated Polyester Fiber Filter by Spray-Coating and Its Photocatalytic Degradation of Gaseous Formaldehyde.* Aerosol and Air Quality Research, 2012. **12**: p. 1327–1335.
154. Aghighi, A. and F. Haghighat, *Evaluation of nano-titanium dioxide (TiO2) catalysts for ultraviolet photocatalytic oxidation air cleaning devices.* Journal of Environmental Chemical Engineering, 2015. **3**(3): p. 1622-1629.
155. Monteiro, R.A.R., et al., *Evaluation of a solar/UV annular pilot scale reactor for 24h continuous photocatalytic oxidation of n-decane.* Chemical Engineering Journal, 2015. **280**(Supplement C): p. 409-416.
156. He, Z., et al., *Treatment of organic waste gas in a paint plant by combined technique of biotrickling filtration with photocatalytic oxidation.* Chemical Engineering Journal, 2012. **200**(Supplement C): p. 645-653.
157. Hüsken, G., M. Hunger, and H.J.H. Brouwers, *Experimental study of photocatalytic concrete products for air purification.* Building and Environment, 2009. **44**(12): p. 2463-2474.
158. Zhong, L. and F. Haghighat, *Photocatalytic air cleaners and materials technologies – Abilities and limitations.* Building and Environment, 2015. **91**: p. 191-203.
159. Krichevskaya, M., et al., *Gas-phase photocatalytic oxidation of refractory VOCs mixtures: Through the net of process limitations.* Catalysis Today, 2017. **280**(Part 1): p. 93-98.
160. Xu, F., et al., *Preparation of photocatalytic TiO2-based self-cleaning coatings for painted surface without interlayer.* Progress in Organic Coatings, 2017. **113**(Supplement C): p. 15-24.

Highlights

- The limitations of the TiO_2-based photocatalyst for photocatalytic degradation of VOCs are reviewed.
- The approaches for modifying TiO_2-based photocatalyst to improve the performance of photodegradation of VOCs are discussed.
- Applications of TiO_2 and modified-TiO_2 photocatalysts for VOCs removal in the gas phase are summarized.
- Fundamental of metal and non-metal doped TiO_2, co-doped TiO_2, and composite TiO_2 with other semiconductors are considered.
- The effects of key controlling parameters on PCO efficiency are reviewed.

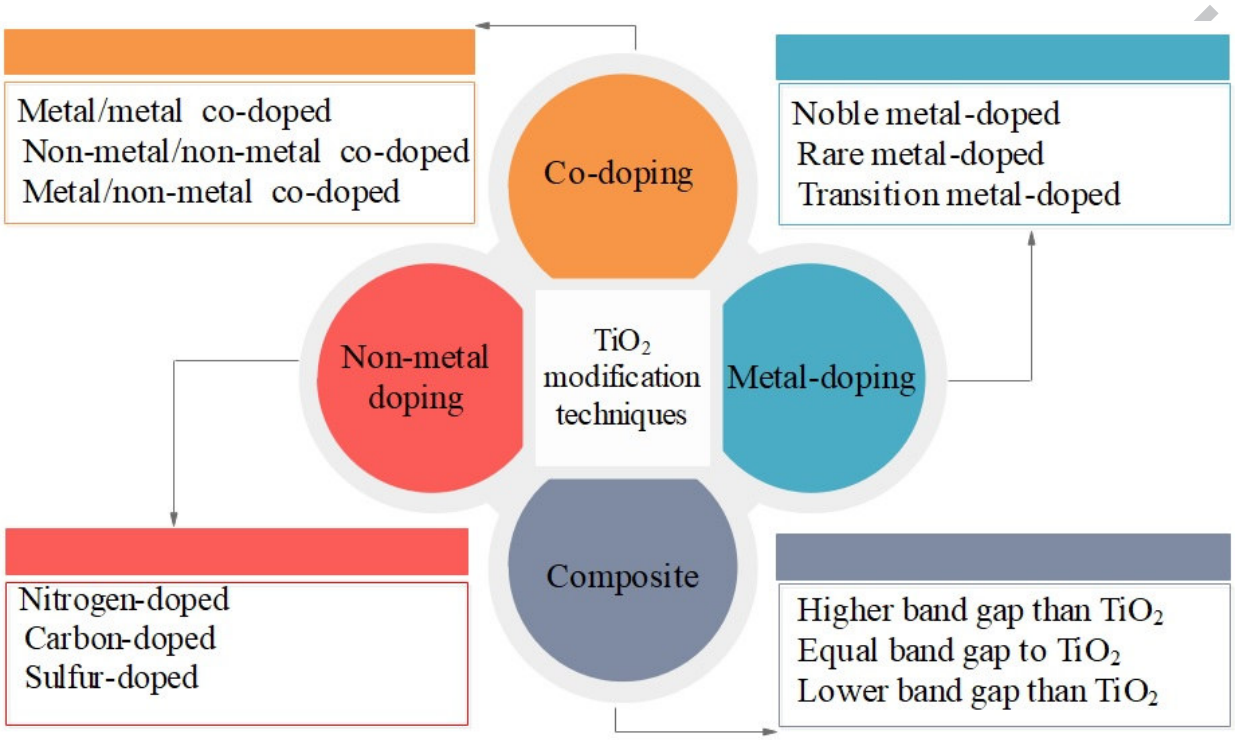
Metal/metal co-doped
Non-metal/non-metal co-doped
Metal/non-metal co-doped
Co-doping
Noble metal-doped
Rare metal-doped
Transition metal-doped
Non-metal doping
TiO2 modification techniques
Metal-doping
Nitrogen-doped
Carbon-doped
Sulfur-doped
Composite
Higher band gap than TiO2
Equal band gap to TiO2
Lower band gap than TiO2

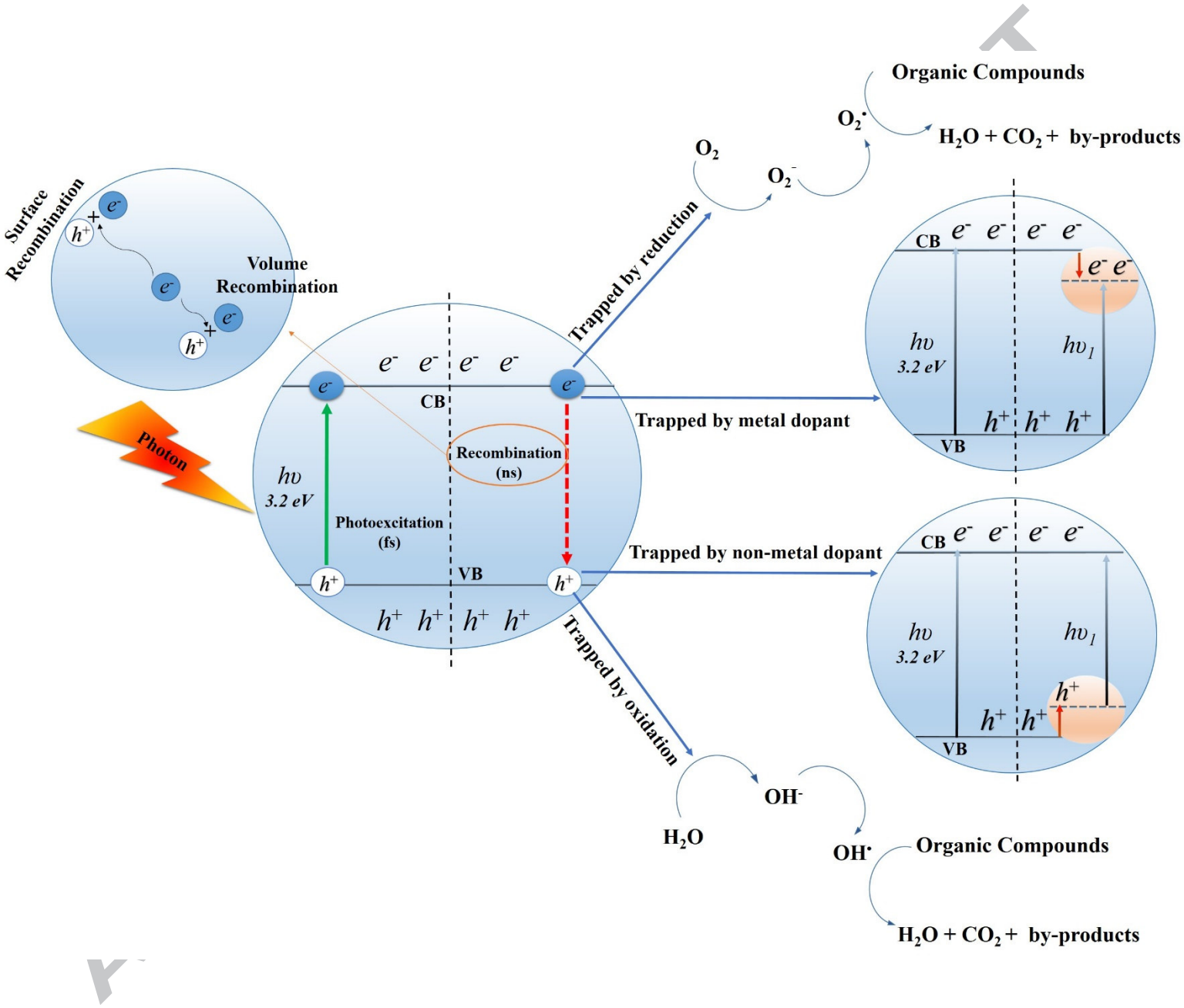

Figure 1. Basic principle of PCO for removal of VOCs.

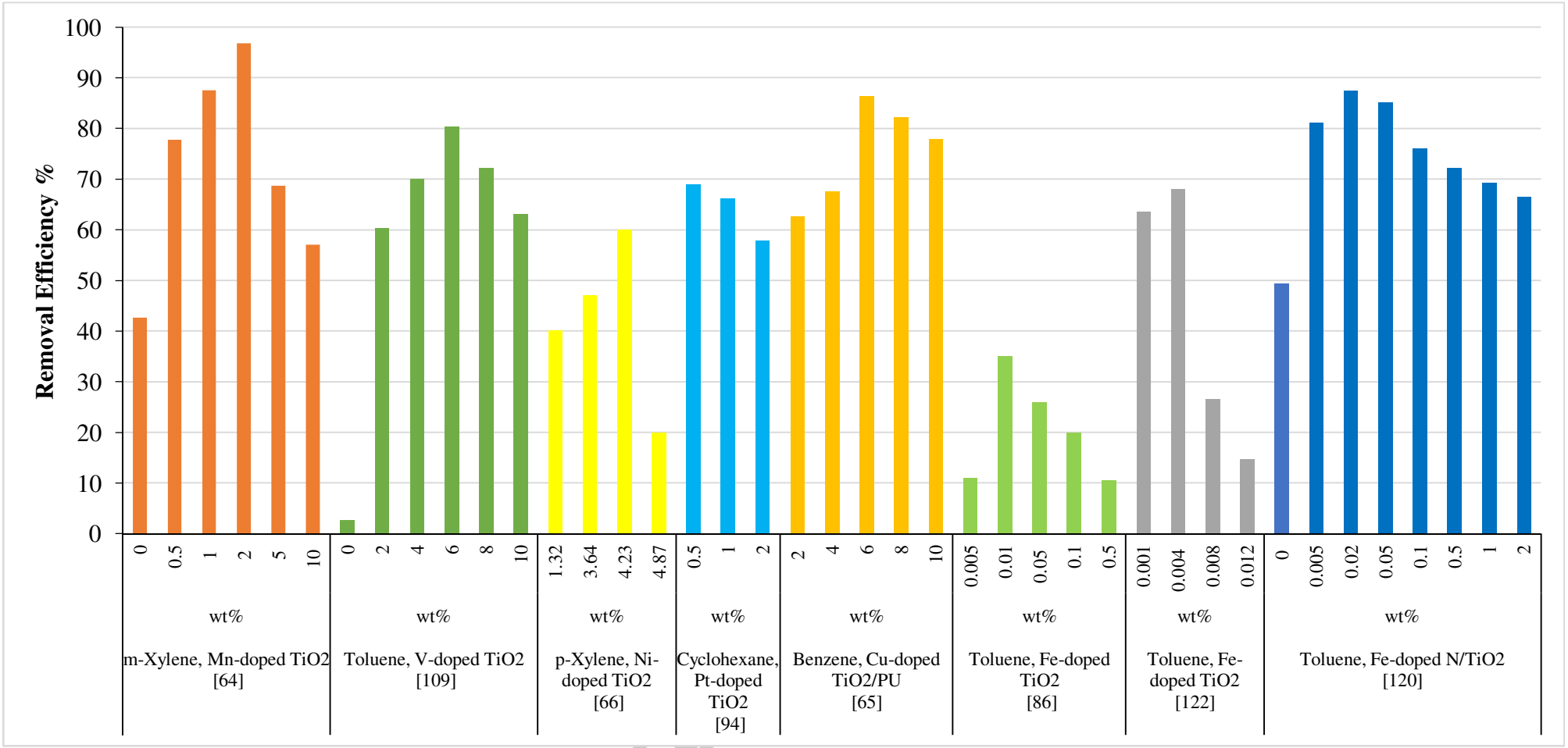

Figure 2. Influence of the amount of different metal dopants (wt.%) on VOCs degradation by TiO_2 photocatalyst.

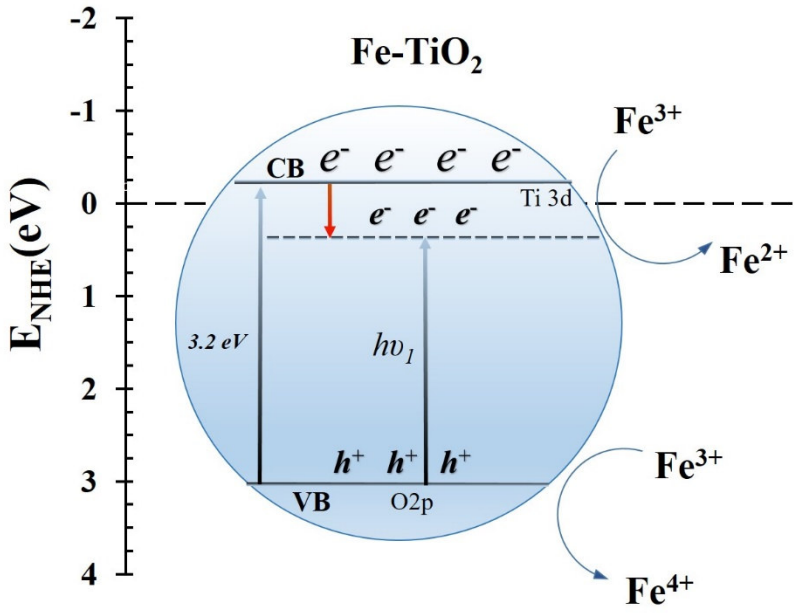

Figure 3. Schematic energy level of Fe (transition metal) doping TiO_2.

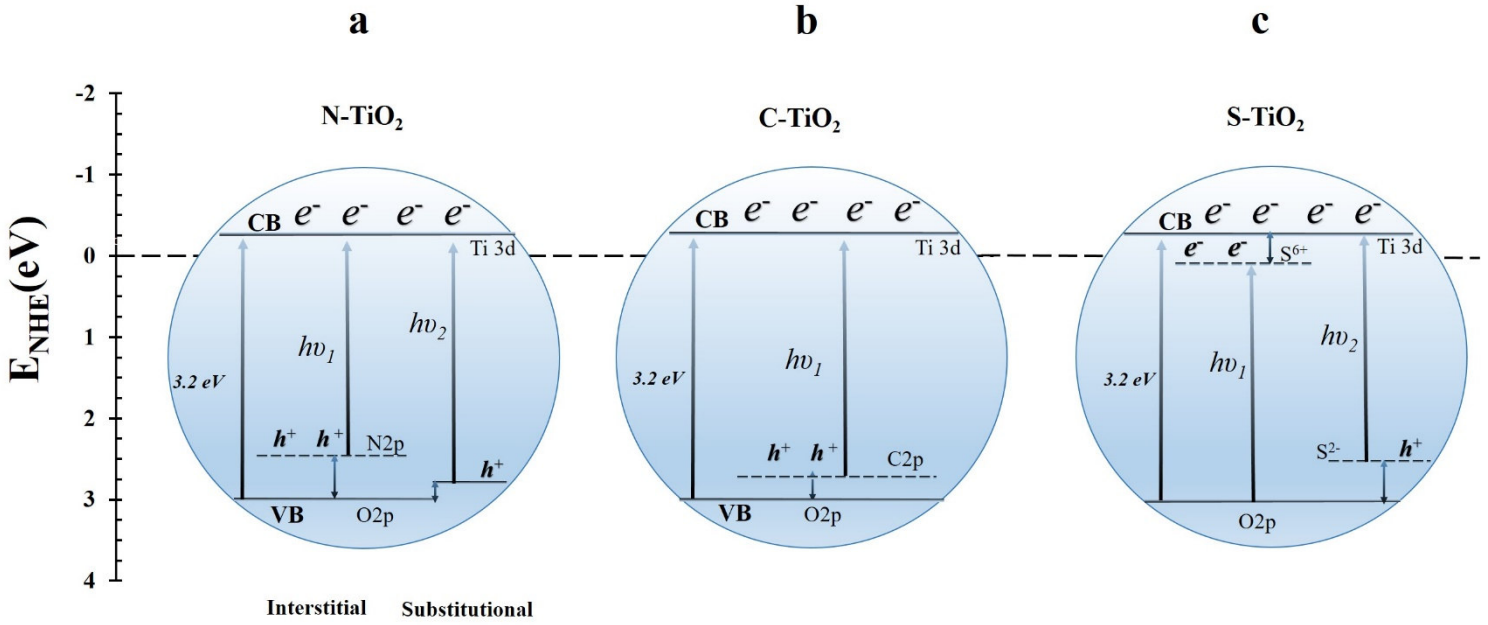

Figure 4. Schematic energy level of (a) N-doped TiO_2, (b) C-doped TiO_2, (c) S-doped TiO_2.

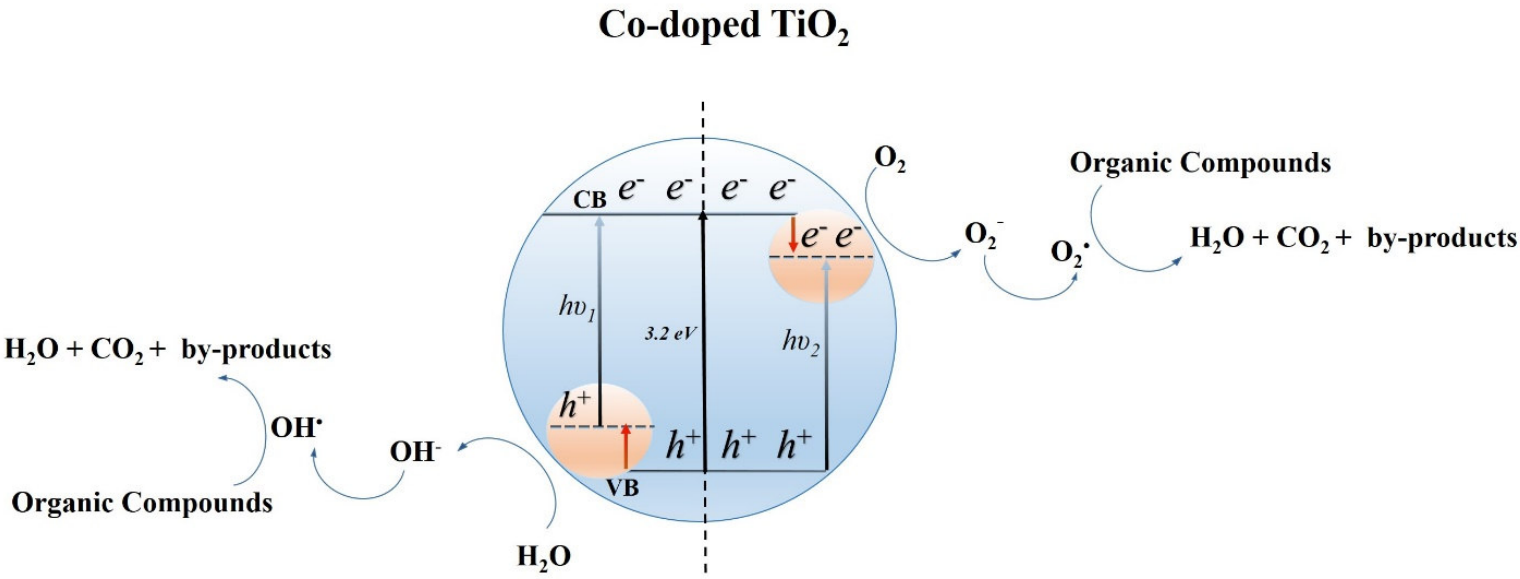

Figure 5. Schematic energy level of metal and non-metal doped TiO_2.

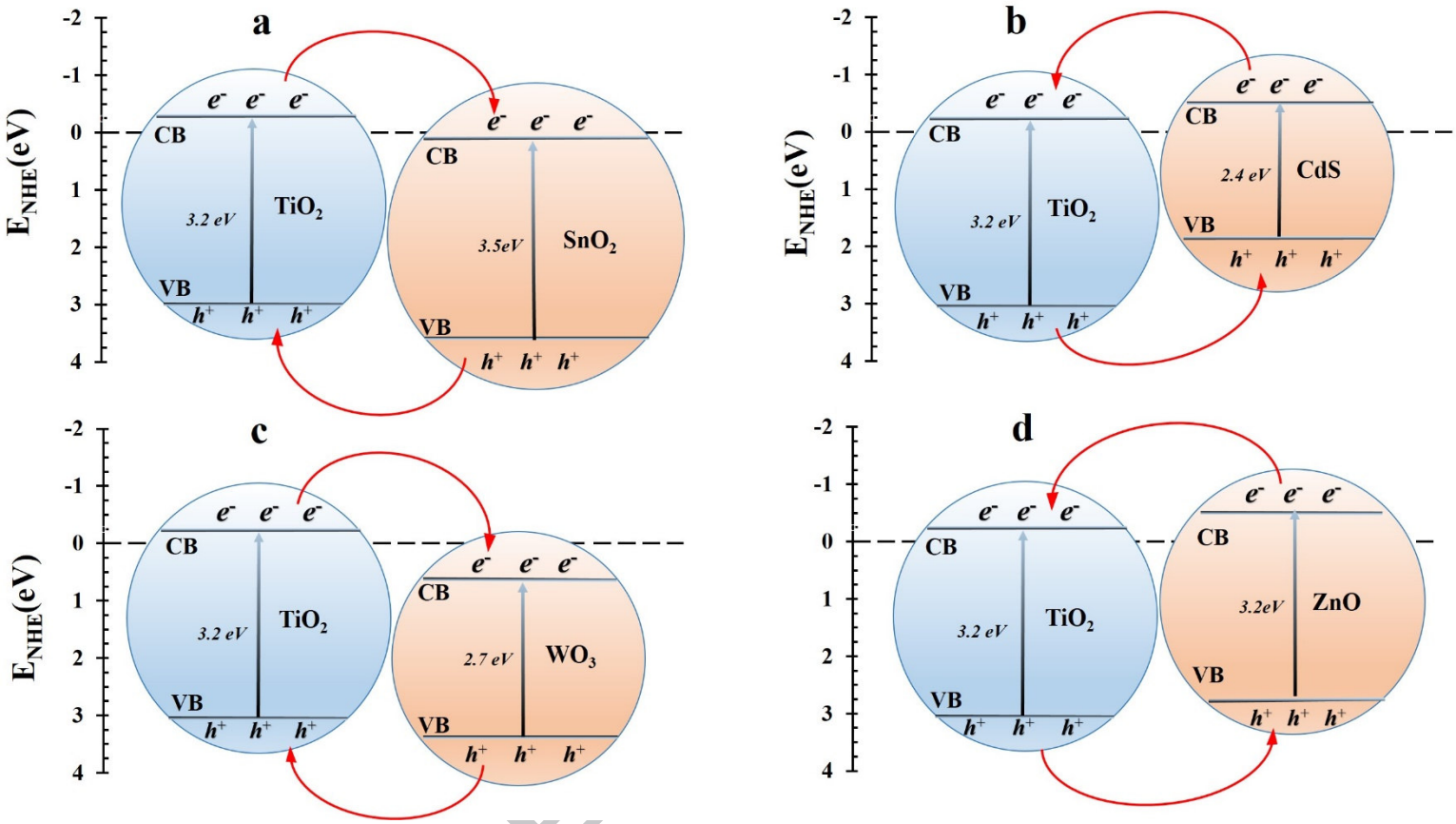

Figure 6. Figure 6. Schematic energy level of TiO_2 composite ***(a)*** *SnO_2 (data extracted from [21, 22, 142]),* ***(b)*** *CdS (data extracted from [140, 142]),* ***(c)*** *WO_3 (data extracted from [106, 142]),* ***(d)*** *ZnO (data extracted from [146]).*

Table 1. The reactions involved in the TiO_2 photocatalytic oxidation process for the degradation of VOC pollutants.

Reactions	Eq. No.
Photoexcitation: $\boldsymbol{TiO_2 + h\vartheta \rightarrow h^+ + e^-}$	1
Oxidation reaction: $\boldsymbol{OH^- + h^+ \rightarrow OH^\bullet}$	2
Reduction reaction: $\boldsymbol{O_{2(ads)} + e^- \rightarrow O^-_{2(ads)}}$	3
Ionization of water: $\boldsymbol{H_2O \rightarrow OH^- + H^+}$	4
Protonation of superoxide: $\boldsymbol{O^{\bullet -}_2 + H^+ \rightarrow HOO^\bullet}$	5
electron scavenger: $\boldsymbol{HOO^\bullet + e^- \rightarrow HOO^-}$	6
Formation of H_2O_2: $\boldsymbol{HOO^- + H^+ \rightarrow H_2O_2}$	7
$\boldsymbol{OH^\bullet + pollutant + O^-_2 \rightarrow products\ (CO_2, H_2O, etc.)}$	8

where h^+ and e^- are hole and electron, respectively.

Table 2. Overview of photocatalytic degradation of VOCs over TiO_2 in various conditions.

Contaminant (concentration)	Photocatalyst	Experimental conditions	Conversion	By-products	Remarks	Ref.
Hexane, Octane, Ethanol, 1-Butanol, Toluene, p-Xylene, Methyl ethyl ketone (MEK) and Acetone (0.25, 0.5, and 1 ppm)	TiO_2; Support: FGFs and CCFs	T= 20-25 °C; RH= 15-45%; AFR= 41–255 m^3/h; Lamps: UVC and VUV; Intensity= 1.6-4.3 $mWcm^{-2}$	TiO_2/CCFs-VUV and 500 ppb; Hexane: 14%; Octane: 15% ; Ethanol: 34% ; 1-Butanol: 41%; Toluene: 20% ; p-Xylene: 22%; MEK: 29%; and Acetone: 25%.	TiO_2/FGFs or CCFs+VUV: • Hexane: formaldehyde, acetaldehyde, 2-butenal, propanal, butanal, tolualdehyde, and hexanal. • Octane: formaldehyde, acetaldehyde, acetone, propanal, butanal and pentanal • Ethanol: formaldehyde, acetaldehyde, 2-butenal, and propanal. • 1-Butanol: formaldehyde, acetaldehyde, 2-butenal, propanal, and butanal. • Toluene: formaldehyde, acetaldehyde, acetone, 2-butenal, butanal, and benzaldehyde. • MEK: formaldehyde, acetaldehyde, acetone, and hexanal. • Acetone: formaldehyde and acetaldehyde.	• Single-pass removal efficiency was varied as: TiO_2/CCFs+VUV>TiO_2/FGFs+VUV>TiO_2/FGFs+UVC. • The lower initial concentrations led to the higher conversion efficiencies.	[7]
Ethylene, Propylene, and Toluene (200 ppm)	TiO_2 (TNPs)	T=25 °C; RH=60%; RT=220 min; Lamps= Combination of UVA (13.6 W) and UVB (3 W)	Ethylene: about 73%; Propylene: about 37%; and Toluene: about 61%	For Propylene: • polyethylene and polypropylene	• Calcination at 400 °C for 3 h were the optimum calcination temperature and time for TNP catalyst • The surface area of the optimized photocatalyst was 3 times higher than Degussa P25 catalyst (53 m^2/g). • An increase in calcination time from 1 to 3 h enhanced the surface area as a result of the absence of impurities and water molecules. • The required surface area for the total adsorbed of toluene is 19.425 m^2/g which is higher than the available 15 m^2/g. This means multilayer adsorption happened during the tested conditions.	[41]

Ethylene, Propylene, and Toluene (200 ppm)	TiO_2 (TNPs)	T=20 to 80 °C; AFR=100 mL/min; Lamps: Combination of UVA (13.6 W) and UVB (3 W)	Ethylene: 66.3%; Propylene: 80.4%; and Toluene: 46%	For Ethylene: • polyethylene and polypropylene. For propylene: • polyethylene and polypropylene. For Toluene: • NA	• Calcination at 400 °C for 3 h were the optimum calcination temperature and time for TNP catalyst • The commercial Degussa P25 showed the lower conversion efficiencies than TNPs. • The highest conversion was achieved at 20 °C. Moreover, by increasing the temperature from 20 to 80 °C, the conversion was decreased. • In the absence of water vapor, the photocatalytic degradation of toluene did not occur. • The toluene illustrated the maximum adsorption capacity on TNP.	[83]
Ethanol (0.25, 0.5, and 1 ppm)	TiO_2; Support: FGFs and CCFs	T=23 °C; RH=15-30%; Lamp: UVC (18.4 W); Intensity= 29-39 $mWcm^{-2}$	17-38% for FGFs+UVC; 19-43% for FGFs+VUV; and 31-53% for CCFs+VUV	NA	• TiO_2/FGFs indicated that for the polar VOCs, the adsorption coefficients were roughly one order of magnitude higher than nonpolar VOCs for a specific RH level. • TiO_2/FGFs filter showed higher adsorption capacity for polar VOCs. • TiO_2/CCFs was better than TiO_2/FGFs in the case of BET surface area, adsorption capacity, resistance against water vapor and photocatalytic activity.	[61]
Toluene (400 ppmv)	Evonik P25, Cristal PC105, Kronos 1077, and Cristal AT-1; Support: Flat glass disk	T=250 °C; RH=40%; Lamp: Iron halogenide lamp (500 W); Intensity = 3 $mWcm^{-2}$	52% (after 6 hr) for P25; 50% (after 6 hr) for PC105; 46% (after 6 hr) for Kronos 1077; and 46% (after 6 hr) for Cristal AT-1	•P-cresol, hydroquinone, benzoic acid, benzaldehyde, benzyl Alcohol, and carbon dioxide.	• Evonik P25 and Cristal PC105 presented high photocatalytic efficiencies and performance within the shorter reaction time. • Micro-sized catalyst shown a higher hydrophilicity/ hydrophobicity ratio	[49]
Toluene (NA)	Nano TiO_2 (Degussa P25); Support: ACFs	T= 25±0.5 °C; RH=15, 30, 45, and 60%; Lamp: UV (15 W 254 nm)	14.2% (RH=60%)	Detected intermediate: • Benzaldehyde (about 74-89%), benzyl alcohol (about 9-19%), benzoic acid (about 1%), 2-methyl, p-benzoquinone (about 1-3%) and cresol (about 1-2%)	• The BET surface area of the original ACFs and TiO_2/ACF were 1215.4 and 999.6 m^2/g, respectively. •Increasing the RH from 15 to 60 % caused increasing in oxidation conversion from 9.5 to 14.2 %. •Accumulation rate of benzyl alcohol increased with the increase of RH, however, accumulation rate of benzaldehyde decreased.	[84]

					• The conversion rate of toluene followed the first-order reaction mechanism.	
Benzene (3.3±0.2 ppmv), Toluene (9.5±0.5 ppmv), Ethylbenzene (9.5±0.5 ppmv), and m-Xylene (15±1 ppmv)	TiO_2; Support: Glass; Coating method: Dip coating	T=NA; RH= 0-35230 ppmv; RT=18-145 s; Lamp: UVC (18 W)	At different RH Benzene: 56-100% (RT~116 s), Toluene: 64-98% (RT~74 s), Ethylbenzene: 65-98% (RT~42 s) and m-Xylene: 68-95% (RT~62 s)	• No by-products were detected above the detection limit (150 ppbv) and CO_2 was the only detected product.	• No conversion of BTEX neither in the case of photolysis (UV irradiation without catalyst) nor catalysis (catalyst without UV irradiation) was observed. • The PCO of toluene and benzene were improved by increasing the water vapor concentration up to the optimum amount, however, the conversions were slightly decreased at more than that concentration. • The increase in residence time led to increase in the conversion.	[56]
Benzene (21.2 ppmv), Toluene (8.57 ppmv), Ethylbenzene (19 ppmv), m-Xylene (10.20 ppmv), o-Xylene (7.53 ppmv), and p-Xylene (23.58 ppmv)	TiO_2	T= 50 ± 2 °C; RH=No humidity; Lamp: Low-pressure Hg (12 W)	Benzene: 82%; Toluene: 97%; Ethylbenzene:83%; m-Xylene: 92%; o-Xylene: 85% and p-Xylene: 98%	• No gas-phase intermediates were detected in the case of benzene, toluene, and ethylbenzene. • Ethylbenzene was produced as by-product in high concentration for m-Xylene while in the case of o,p-Xylene was produced in low concentration.	• Adsorption on the catalyst surface for aromatic compounds was in the following order: Toluene>m-Xylene>p-Xylene>o-Xylene>Benzene> Ethylbenzene •	[85]
Benzene (~47 ppm), Toluene (~42 ppm), Ethylbenzene (~39 ppm), p,m-Xylene (~41ppm), and o-Xylene (~27 ppm)	TiO_2; Support: glass	T= 30.1 ± 0.7 °C; RH=42.2 ± 3.2%; RT= 7.0 ± 0.25 min; Lamps: UVC (8,11,16 W, 254 nm)	Benzene: 82.8%; Toluene: 35.8%; Ethylbenzene: 97.9%; p,m-Xylene: 58.9% and o-Xylene: 67%	• High formation of intermediates for toluene degradation such as benzaldehyde and benzoic acid led to decrease degradation rate constant much faster than the other considered VOCs.	• The particle size of TiO_2 was 10.2±1.43 nm and uniformly dispersed on the surface of the catalyst. • By decreasing the particle size specifically under the 30 nm, the photocatalytic activity of TiO_2 and the number of active surface sites increased. • The BET surface area of the catalyst powder was 9 m^2/g.	[28]
Benzene (25ppmv)	TiO_2; Support: Zeolite (ZSM-5 with Si/Al of 200 and 470, MCM-41);	T= NA; RH=50%; AFR= 1 L/min; Lamps: Two VUV (4 W), Two UVC	100% for TiO_2/ZSM-5 (250 min) and 95% (360 min) 100% for TiO_2/MCM-41 (180 min) and 87% (360 min)	NA	• No considerable rutile phase was detected in the XRD pattern of TiO_2/MCM-41. However, the small diffraction peak of rutile phase was observed on TiO_2/ZSM-5 (200) and TiO_2/ZSM-5 (470).	[77]

		(4 W, 254 nm)			• The stable benzene degradation efficiency for the various catalysts followed the order: TiO_2/ZSM-5(200)>TiO_2/ZSM-5(470)>TiO_2/MCM–41>P25. • TiO_2/ZSM-5(200) displayed the highest CO_2 concentration which is represented that it was a reliable catalyst for ozone degradation. • All the supported TiO_2 catalysts demonstrated higher photoactivity for benzene removal.	
Acetone and Acetaldehyde (400 ppmv)	Evonik P25, Cristal PC105, Kronos 1077, and Cristal AT-1; Support: Flat glass disk	T=250 °C; RH=40%; Lamp: Iron halogenide lamp (500 W); Intensity= 3 $mWcm^{-2}$	Acetone: 100% (after 70 min) for P25, 100% (after 60 min) for PC105, 100% (after 90 min) for Kronos 1077, and 49% (after 120 min) for Cristal AT-1 Acetaldehyde: 100% (after 60min) for P25, 100% (after 50min) for PC105, 100% (after 70min) for Kronos 1077, and 46% (after 120 min) for Cristal AT-1	Acetone: • No by-product in the case of Evonik P25, Cristal PC105 and Kronos 1077. • By-products for Cristal AT-1 were acetaldehyde, acetic acid, formaldehyde, formic acid, and carbon dioxide. Acetaldehyde: • No by-product in the case of Evonik P25, Cristal PC105 and Kronos 1077.	• Evonik P25 and PC105 presented high photocatalytic efficiency and performance within the shorter reaction time. • Micro-sized catalyst had a higher hydrophilicity/ hydrophobicity ratio.	[49]

T: Temperature
RH: Relative Humidity
AFR: Air Flow Rate
RT: Residence Time
NA: Not Available
TNP: Titanium nanoparticle
FGFs: Fiberglass fibers
CCFs: Carbon cloth fibers
ACFs: Activated carbon fibers

Table 3. Common preparation method of modified TiO_2 photocatalyst for PCO.

	Synthesize Method	Photocatalyst	Precursor	Dopant/source	Ratio (dopant/ TiO_2)	Treatment Temp./Duration	Cal. Temp./ Duration	Ref.
Metal	Sol-gel	Mn-doped,	Tetra butyl titanate	Mn, Cu, Co, Ni, and Fe	1%	120 °C /6 h	550 °C /4 h	[79]

doping		Cu-doped, Co-doped, Fe-doped, Ni-doped		/Acetate of transition metals				
		Fe-doped	Tetra butyl titanium	Fe/ Iron (III) nitrate	Fe/Ti atomic ratio: 0.1% to 1.5%	80 °C /48 h	480 °C /3 h	[73]
		Fe-doped	Tetra-n-butyl titanium	Fe/ Iron (III) nitrate	Fe/Ti ratios: 0.005, 0.01, 0.05, 0.1, and 0.5	Room Temp. /3 h	400 °C /1 h	[86]
		Fe-doped	Titanium tetraiso-propoxide	Fe/ Iron (III) acetylacetonate	Fe/Ti molar ratios: 0.001 to 0.1%	350–450 °C /4 h	NA	[90]
		Pt-doped	Titanium tetraisopropoxide	Pt/ Hexachloroplatinic acid	0.5 and 1 wt.%	110 °C / overnight	650 °C /2 h	[91]
		Ni-doped	Titanium butoxide	Ni/ Nickel (II) chloride	0.1, 0.3, and 0.5 wt.%	110 °C /12 h	500 °C /5 h	[21]
	Hydrothermal	Ce-doped, Fe-doped, Ni-doped	Tetra butyl titanate	Ce/ Cerium (III) nitrate Fe/ Iron (III) nitrate Ni/ Ni (II) nitrate	0.5 and 5 wt.%	80 °C /24 h	500 °C /2 h	[92]
	Impregnation	Mn-doped	Titanium (IV) butoxide	Mn/ Manganese nitrate	0.5 to 10 wt.%	80 °C / overnight	500 °C /3 h	[62]
		Pt-doped	P25 Degussa	Pt/ Chloroplatinic acid	0.1 and 1 wt.%	120 °C /4 h	400 °C /4 h	[93]
	Hydrolysis	Pt-doped	Titanium tetraiso-propoxide	Pt/ Chloroplatinic acid	0.5, 1 and 2 wt.%	NA	650 °C /2 h	[94]
		Ru-doped	Titanium oxosulphate	Ru/ Ruthenium chloride	0.005, 0.01, 0.05, 0.1, 0.25, 0.5, and 0.75 g	100 °C /8 h	600 °C /2 h	[95]
	Thermal assisted microwave	Ir-doped	Titanium (IV) ethoxide	Ir/ Iridium (III) chloride	0.25, 0.5, 0.75, and 1.5 wt.%	60 °C /24 h	200 °C /7 min. 500 W	[96]
Non-metal doping	Sol-gel	B-doped	Titanium butoxide	B/ Boric acid	1, 3, and 5 wt.%	110 °C /12 h	500 °C /5h	[23]
		C-doped	Tetra-titanium-isopropoxide	C/ Carbon particle	NA	Room Temp. /12 h	400 °C /1 h	[97]
	Hydrothermal	C-doped	Titanium (IV) Sulfate	C/ Glaucous	C/Ti molar ratio: 3:50, 1:50, and 1:150	160 °C /12 h	NA	[38]
		C-doped	Titanium (IV) Sulfate	C/ Sucrose	1:25	180 °C /12 h	NA	[98]
		C-doped	Ammonium hexafluorotitanate	C/ Glaucous	NA	180 °C /24 h	500 °C	[99]
		N-doped	Tetra butyl titanate	N/ ammonia	NA	NA	600 °C /2 h	[19]

	Thermal treatment	N-doped	P25 powder	N/ Ammonium hydroxide	NA	NA	400 °C /3 h	[100]
	Microemulsion	S-doped	Titanium (IV) isopropoxide	S/ Ammonium sulfate	S/Ti molar ratio: 1, 5, and 20%	110 °C /24 h	600 °C /2 h	[87]
	Hydrolysis	S-doped	Degussa P25	S/ Thiourea	Si/Ti ratio: 0.2, 0.4, 0.8, and 1.6	85 °C /20 h	450 °C /4 h	[101]
	Impregnation	F-doped	P25 powder	F/ ammonium fluoride	mass ratios of 0.3 NH_4F/ TiO_2	85 °C /8 h	500 °C /3 h	[100]
	Solvothermal	S-doped	Titanium isopropoxide	S/Thiourea	molar ratio Ti/S of 1:4	Room Temp. /2 days	350 °C	[102]
Co-doping	Sol-gel	B, Fe co-doped	Titanium butoxide	B/ Boric acid Fe/ Iron (III) acetylacetonate	B: 3 wt.% Fe:0.5, 1, 3, and 5 wt.%	110 °C /12 h	500 °C /5 h	[23]
		F,N co-doped	Titanium tetraisopropoxide	F/ ammonium fluoride N/ ammonium hydroxide	NA	85 °C /8 h	500 °C /3 h	[100]
	Impregnation	Na-doped Pd/TiO_2	Degussa P25	Pd/ Palladium (II) nitrate Na/ Sodium nitrate	Pd:1 wt.% Na: 1, 2, 4, and 8 wt.%	110 °C / overnight	400 °C /2 h	[103]
	Microemulsion	Fe, S co-doped	Titanium (IV) isopropoxide	S/ Ammonium sulfate Fe/ Iron(III) nitrate	S/Ti molar ratio:1, 5, and 20% Fe/Ti molar ratio:1.5%	110 °C /24 h	600 °C /2 h	[87]
	Hydrolysis	C, N, and S tri-doped	Titanium isopropoxide	Thiourea	molar ratio of thiourea to TiO_2 is 0, 1, 2, 3 and 6	80 °C /10 h	500 °C /3 h	[104]
Composite	Sol-gel	N doped TiO_2-Nb_2O_5 composit	Titanium isopropoxide	N/ Ammonium hydroxide Nb_2O_5/ potassium niobate	N: 0.49 at.% TiO_2: 50 wt.% Nb_2O_5: 50 wt.%	80 °C	380 and 500 °C /5 h	[25]
		SiO_2 -TiO_2 Composite	Titanium n-butyloxide	Si/ Tetraethoxysilane (TEOS)	Si/Ti molar ratio:1:100, 5:100, 10:100, 15:100, and 20:100	130 °C /8 h	500 °C	[37]
		ZnO-TiO_2 Composite	Titanium isopropoxide	ZnO/ Zinc acetate	50 wt % of ZnO and 50 wt.% of TiO_2	80 °C /48 h	380 and 500 °C /5 h	[105]
	Impregnation	Ni–TiO_2–SnO_2	Titanium butoxide	Ni/ Nickel (II) chloride SnO_2/ Triphenyltin hydroxide	Ni: 0.1, 0.3, and 0.5 wt.%	Room Temp/24 h	500 °C /5 h	[21]
		N-TiO_2/WO_3	Titanium tetraisopropoxide	N/Urea WO_3/ Ammonium paratungstate	N/ WO_3/ TiO_2 compositions: 2.5/ 0.5/ 100, 2.5/1.0/	110 °C /2 h	350 °C /2 h	[106]

				pentahydrate	100, 2.5/2.0/ 100, 2.5/4.0/ 100, and 2.5/6.0/ 100			

Cal.: Calcination;
Temp.: Temperature;
NA: Not Available.

Table 4. Summary of the common noble and transition metal dopants in the TiO_2 photocatalyst with their operated photocatalytic conditions and maximum efficiencies.

Contaminant (Concentration)	Photocatalyst	Dopant	Experimental condition	Efficiency before doping	Efficiency after doping	Band gap	Remarks	Ref.
BTEX (0-22 ppmv)	Pt- doped P25, Fe-doped P25, Ce-doped P25; Support: glass; Method: Wet impregnation	Pt, Fe, and Ce: 0.25 % (w/w)	RT=11.5±0.5 s; Lamp: Low-pressure Hg, UVC, 11 W (253.7 nm)	Benzene: 10-28%; Toluene: 2-12%; Ethylbenzene: 4-59%; and m-Xylene: 6-87%	Benzene: 4.6-6.5% for Pt/P25, 4.6-12% for Fe/P25, and 17-79% for Ce/P25; Toluene: 3-9% for Pt/P25, 2.7-6% for Fe/P25, and 3-9% for Ce/P25; Ethylbenzene: 15-89% for Pt/P25, 5-80% for Fe/P25, and 10-92% for Ce/P25; m-Xylene: 9-83% for Pt/P25, 6-81% for Fe/P25, and 9-86% for Ce/P25	NA	• In the case of PCO of benzene, only Ce/P25 catalyst was efficient. • PCO rates over P25/Ce were higher by a factor of 1.5-10 than those over P25. • For PCO of toluene, P25 catalyst proved to be the most active. • For PCO of ethylbenzene, all doped catalysts followed the same trend. • For all ethylbenzene concentration range, the P25/Ce catalyst was superior to others. • In the case of m-xylene, there was no catalyst superior to the others at all concentration range. • The PCO conversions of ethylbenzene and m-xylene indicated a great dependence on the initial concentration of the target compound.	[113]
BTEX (0.1 ppm)	Fe-doped TiO_2; Support: Glass Fiber; Synthesize method: Sol-gel;	Fe-to Ti ratio: 0.005, 0.01, 0.05, 0.1, and 0.5	T=NA; RH=45%; AFR=1 L/min; Lamp: UVA-visible	Under visible light: 0% for Benzene; 5% for	Visible light and 0.01-GF-Fe-TiO_2 Benzene: 4%; Toluene: 33%; Ethylbenzene: 51% and	NA	• The calculated diameter of TiO_2 crystal was 21.5 nm which was similar to the calculated diameters of the Fe-TiO_2 composites (20.9–21.7 nm). • The GF-Fe-TiO_2 composites showed higher photocatalytic activity for BTEX rather than the GF-TiO_2 (reference) photocatalyst.	[86]

	Coating method: Dip-coating		(daylight and black light lamp); Visible light intensity= 2.7 $mWcm^{-2}$ and UV light intensity= 0.4 $mWcm^{-2}$	Toluene; 16% for Ethylbenzene and 29% for o-Xylene Under UV light: 68% for Benzene, 90% for Toluene, 96% for Ethylbenzene, and 97% for o-Xylene	o-Xylene: 74% UV light and 0.5-GF-Fe-TiO_2 Benzene: 15%; Toluene: 63%; Ethylbenzene:79% and o-Xylene: 86%		• The photocatalytic activities of BTEX for GF-Fe-TiO_2 under visible light reduced gradually by increasing the Fe-to-Ti ratio from 0.01 to 0.50. • The BTEX photocatalytic efficiencies of GF-Fe-TiO_2 under UV were lower than those obtained for GF-TiO_2. • The GF-TiO_2 photocatalyst demonstrates an absorption edge at $\lambda \approx 410$ nm.	
Benzene (50 ppmv)	R-doped TiO_2 (R: Mn, Co, Cu, Fe, and Ni), undoped TiO_2 and P25; Synthesize method: Sol-gel	Mn, Co, Cu, Fe, and Ni 1wt.%	T=NA; RH=50%; AFR=1 L/min; RT=30 s; Lamps: UVC and VUV, 4 W	45.7% for undoped TiO_2 and 50.2% for P25	58% for Mn/TiO_2; 51.5% for Co/TiO_2; 50.9% for Cu/TiO_2; 45.3% for Fe/TiO_2 and 50.3% for Ni/TiO_2 (Under VUV)	NA	• BET surface area of pure TiO_2 was 96.6 m^2/g while it declined to less than 50 m^2/g for all doped catalysts. • It is possible that the presence of transition metals blocked the pores of TiO_2 and increase the growing of particles which lead to the reduction of specific surface area.	[79]
Benzene (100 ppm)	Cu-doped TiO_2; Support: Porous polyurethane (PU)	Cu: 2, 4, 6, 8, and 10 wt.%	T= NA; RH=40, 60, 80%; AFR= 100 mL/min; Lamps= two 20 W light bulbs (400-700 nm); Intensity= 50 $mWcm^{-2}$	NA	86.3% for 6 wt.%-Cu-TiO_2/PU	3.20 eV for TiO_2/PU; 3.05 eV for 2 wt.% -Cu-TiO_2/PU; 2.92 eV for 4 wt.% -Cu-TiO_2/PU; 2.85 eV for 6 wt.% -Cu-TiO_2/PU; 2.79 eV for 8 wt.% -Cu-TiO_2/PU and 2.75 eV for 10 wt.%-Cu-TiO_2/PU	• Optimal humidity conditions for the photocatalytic oxidation of benzene in Cu–TiO_2/PU photocatalyst, was 60% RH. • Water molecules played an important role in the photocatalytic oxidation process of benzene. • The Cu^+/Cu^{2+} ratios, the benzene removal efficiency and the degree of mineralization enhanced with the increase in the Cu/TiO_2 ratios reached up to 6 wt%, and then gradually decreased with the further increase in ratios (8 and 10 wt%).	[63]
Toluene (370 ppmv)	Fe-doped TiO_2; Support: glass fiber;	Fe (Fe/Ti atom	T=Room temperature; RH=60%;	Efficiency NA	Efficiency NA 40-96.5%	3.18 eV for 0.1%-Fe-TiO_2;	• No degradation of toluene was observed on the surface of the catalyst in absence of irradiation. • Only about 5.8% of the toluene was converted	[73]

	Synthesize method: Sol gel	ratio: 0.1-1.5%)	Lamp: UV-visible, 300 W (UV cut-off filter)	14.9% mineralization for TiO_2	mineralization (Maximum for Fe/Ti ratio of 0.7%)	3.12 eV for 0.3% Fe-TiO_2; 3.08 eV for 0.5% Fe-TiO_2; 3.02 eV for 0.7% Fe-TiO_2; 3.00 eV for 1.0% Fe-TiO_2 and 2.96 eV for 1.5% Fe-TiO_2	after 2h irradiation without the photocatalyst. • By increasing Fe concentration to reach Fe/Ti ratio of 0.7%, the degradation rate of toluene increased significantly and reached the maximum level. Further Fe concentration led to a gradual decrease of the degradation rate. • The Fe ion could replace with Ti^{4+} ions in TiO_2 lattice which leads to extend the photoactivity of TiO_2 to visible range and increase the electron and hole pairs' formation.	
Toluene (120 ppm)	Ag-doped TiO_2 nanotube	Ag 1 wt.%	T=NA; RH=NA; Lamps: UV (8W) and visible light (500W Xe); UV light intensity= 0.87 $mWcm^{-2}$ Visible light intensity= 0.87 $mWcm^{-2}$	79% for P25 (after 6 h) 90% for pure TiO_2 under UV	98% (after 4 h) under UV	NA	• By doping Ag into the TiO_2 nanotubes, the density of surface defects was increased and acts as rutile nucleation sites and result in promoting of phase transfer. • The concentration of surface oxygen vacancy of anatase particles was improved in the Ag-doping TiO_2 nanotubes, which caused Ag dopant could promote the transformation of anatase to rutile phase at lower calcination temperature. • The surface area of 1% Ag-doping TiO_2 nanotubes was 78.5 $m^2 g^{-1}$ and it was higher than P25 (52 $m^2 g^{-1}$). • The pore size distribution of the catalyst was in the range of 1.0 and 30 nm, however, the main pore volume was found in the mesopores with diameters varying from 1.4 to 20 nm.	[114]
Toluene (200 ppm)	V-doped TiO_2	V: 0, 2, 4, 6, 8 and 10 wt.%	T=NA; RH=50%; AFR= 200 mL/min; Lamp: visible light, 20 W (400-700 nm); Intensity= 50 $mWcm^{-2}$	About 2% for undoped TiO_2	80% for 6 wt.% V-TiO_2	3.20 eV for TiO_2/PU; 3.09 eV for 2 wt.% -V-TiO_2/PU; 2.93 eV for 4 wt.% -V-TiO_2/PU; 2.83 eV for 6 wt.% -V-TiO_2/PU; 2.76 eV for 8 wt.% -V-TiO_2/PU and 2.70 eV for 10 wt.%-V-TiO_2/PU	• The optimum value for V content in V/TiO_2 catalyst which showed the highest photocatalytic activity and high mineralization was 6 wt%. • The band gap energy of V-TiO_2/PU was gradually decreased with increase in the V/TiO_2 ratios.	[109]
p-Xylene (80 ppm),	Ni doped TiO_2 and Degussa	Ni: 0, 1.32,	T=NA; RH=30-	p-Xylene: 33%,	p-Xylene: about 20-60%;	NA	• The concentration of xylene did not change with photolysis (under UV irradiation without	[64]

m-Xylene (70 ppm), and o-Xylene (60 ppm)	P25; Support: Granular silicate glass; Coating method: impregnation	3.64, 4.23, 4.87, 4.46, 4.57, and 4.74 wt.%	90%; RT= 54 s; Lamp: UVC, 10 W (254 nm)	m-Xylene: 35%, and o-Xylene: 32%	m-Xylene: about 18-58%; and o-Xylene: about 18-54%		photocatalyst) or catalysis (under dark conditions in the presence of the photocatalyst). • The photocatalytic degradation of xylene over TiO_2 can be improved by doping Ni at a concentration lower than 4.2 wt.%, otherwise, the photocatalytic activity of modified TiO_2 would be worse than that of pure TiO_2.	
m-Xylene (207 ppb)	Mn-doped TiO_2	Mn: 0.5, 1, 2, 5, and 10 wt%	T=100 °C; RH=23-25% and 75-80%; RT=0.55-3.11s; AFR=12 L/min; Lamp: UV lamp	33.5±4.8%	2wt.%-Mn-TiO_2 50±3.3 %	3.2 eV for TiO_2; 3.1 eV for 0.5 wt.%-Mn-TiO_2; 3.06 eV for 1 wt.%-Mn-TiO_2; 3.01 eV for 2 wt.%-Mn-TiO_2; 2.8 eV for 5 wt.%-Mn-TiO_2 and 1.2 eV for 10 wt.%-Mn-TiO_2	• The loaded Mn provided more active sites on the photocatalyst surface, thus increased the photocatalytic activity. • Mn-doped TiO_2 results in narrowing the band gap. • Mn dopants ions caused to reduce the charge carrier recombination rate and improved the separation rate of electron–hole pairs. • Removal efficiency increased by loading Mn up to 2 wt%. However, an excess amount of Mn on the surface of catalyst led to decreeing in removal efficiency.	[62]
Isopropanol (1100 ppm)	Rare earth-doped TiO_2 (RE= cerium, lanthanum, europium and yttrium), Undoped P25; Method: Thermal treatment (Cal. Temp: 900 and 1000 ºC	Ce, La, Eu, and Y: 0.01 and 0.025 mol	T=23±2 °C; RH=25-30%; Lamp: Xenon lamp, 300 W (400-800 nm); Intensity= 16 $mWcm^{-2}$	Efficiency NA [Acetone formation (ppm h^{-1}) at Cal. Temp:900 For P25= 15]	Efficiency NA [Acetone formation (ppm h^{-1}) at Cal. Temp:900 for La (0.01 mol)=26; La (0.025 mol)=32; Eu (0.01 mol)=27; Eu (0.025 mol)=19; Y (0.01 mol)=18; Y (0.025 mol)=21; Ce (0.01 mol)<0.5 and Ce (0.01 mol)<0.5]	3.01 eV for P25; 3.04 eV for La (0.01 mol); 3.04 eV for La (0.025 mol); 3.03 eV for Eu (0.01 mol); 3.04 eV for Eu (0.025 mol); 3.03 eV for Y (0.01 mol); 3.03 eV for Y (0.025 mol); 2.91 eV for Ce (0.01 mol) and 2.90 eV for Ce (0.025 mol)	• The thermal treatment of the undoped P25 powder, caused to a decrease of its photocatalytic activity due to the concomitant size growth of the titania particles, and the decrease of its specific surface area. • The three catalysts La (0.025 mol)-900, Eu (0.01 mol)-900 and La (0.01 mol)-900 all had high photocatalytic activity under visible-light irradiation. • The rare earth doped TiO_2 modifications led to attach more hydroxyl groups to the surface of the photocatalyst and generate chemical oxidative species, such as hydroxyl radicals which enhanced the photocatalytic activity.	[124]
Ethanol (0.2 vol. %) (Concentration of 0.2 vol.%, in	Pt-doped TiO_2	Pt: 0.5 and 1 wt.%	T=60,80, and 100 °C; RH=NA; AFR=20-70 L/h; Lamps= two	For undoped TiO_2: 69%, 82% and 80% (at 60, 80, and 100 °C,	98% for 0.5wt.%-Pt/TiO_2 (at 80 °C) and 80% for 1 wt.% Pt/TiO_2 (at 80 °C)	3.2 eV for TiO_2; 2.8 eV for 0.5 wt.%-Pt-TiO_2 and 3.0 eV for 1 wt.%-Pt-TiO_2	• No ethanol conversion was observed in dark adsorption for all tested temperature (60, 80 or 100 °C). • The conversion of ethanol enhanced when the reaction temperature increased to 80 °C and then decreased for the reaction temperature of 100 °C.	[91]

helium flow with an oxygen/ethanol ratio of 2)			UVA-LEDs modules (Each module consisted of 40 UV-LEDs, 365nm); Intensity= 90 $mWcm^{-2}$	respectively)			• Ethanol conversion achieved with the catalysts with 1 wt.% Pt was slightly lower than those obtained with 0.5 wt.% Pt. • Acetaldehyde was the main reaction product observed in all tests.	
Acetonitrile (500 ppm)	M-doped TiO_2 M: V, Cr, Fe, Co, Mn, Mo, Ni, Cu, Y, Ce, and Zr	Ti/M=20 atomic ratio (M: V, Cr, Fe, Co, Mn, Mo, Ni, Cu, Y, Ce, and Zr)	T=30-33 °C; RH=NA; AFR=100, 200, 300, and 500 mL/min; Lamps: Six fluorescent white light lamps, 8W	4.5% for P25	70% for Cr-TiO_2; 21% for Fe-TiO_2; 3.3% for Co-TiO_2; 3.5% for Ce-TiO_2; 5% for Cu-TiO_2; 16.5% for V-TiO_2; 2% for Ni-TiO_2; 3.5% for Mn-TiO_2; 2.3% for Mo-TiO_2; 4.5% for Zr-TiO_2 and 3% for Y-TiO_2	3.11 eV for P25; 2.82 eV for Cr-TiO_2; 2.69 eV for Fe-TiO_2; 2.54 eV for Co-TiO_2; 3.13 eV for Ce-TiO_2; 2.86 eV for Cu-TiO_2; 2.63 eV for V-TiO_2; 2.37 eV for Ni-TiO_2; 2.86 eV for Mn-TiO_2; 3.19 eV for Mo-TiO_2; 3.21 eV for Zr-TiO_2 and 3.20 eV for Y-TiO_2	• The Cr, Fe and V-doped TiO_2 nanoparticles showed better photocatalytic efficiency under the visible light. • The incorporation of the other transition metals including Mn, Mo, Ce, Co, Cu, Ni, Y, and Zr demonstrated an inhibition effect on the photocatalytic activity. • Cr-doped TiO_2 exhibited a superior photocatalytic activity and the rate constant for this modified catalyst was about 8–19 times higher than the other tested metal doped catalysts.	[125]
Acetaldehyde (500 ppm) and Toluene (100 ppm)	Ir-doped TiO_2; Support: glass dish; Coating method: Spray Coating	Ir: 0.25, 0.5, 0.75, and 1.5 wt.%	T= Room temperature; Lamp: LED (455 ± 0.1 nm); Intensity= 1 $mWcm^{-2}$	Efficiency NA [About 270 CO_2 ppm for undoped TiO_2]	Efficiency NA [500 ppm CO_2 for 0.5 wt% Ir-doped TiO_2]	3.14 eV for bare TiO_2 (brookite) and 1.88 eV for 0.5wt.%-Ir-TiO_2	• The specific surface areas for 0.25, 0.5, 0.75 and 1.5 wt% Ir-doped TiO_2 brookite corresponded to 172.13, 208.41, 219.67, and 231.15 m^2g^{-1} respectively, and for the undoped brookite was 128.18 m^2g^{-1}. • 0.5 wt% Ir-doped TiO_2 had the highest photocatalytic activity for decomposition of both acetaldehyde and toluene. • The band gaps of the undoped and 0.5wt% Ir-doped TiO_2 catalyst were 3.14 eV and 1.88 eV respectively.	[96]
Acetone (NA)	Ru-doped TiO_2	Ru: 0.75, 0.5, 0.25, 0.1, 0.05, 0.01 and 0.005 g	Lamps: UV (365 nm and 400 nm)	Efficiency NA [Rate constant for P25 Degussa was 0.00041]	Efficiency NA [Rate constant for 0.05-Ru-TiO_2 was 0.00059 and for 0.01-Ru-TiO_2 was 0.00058]	3.2 eV for TiO_2; 2.7 eV for 0.75g-Ru-TiO_2; 2.9 eV for 0.5g-Ru-TiO_2; 2.9 eV for 0.25g-Ru-TiO_2; 2.9 eV for 0.1g-Ru-TiO_2;	• The photocatalytic activities of Ru-doped TiO_2 catalysts under visible light were strongly affected by the decreasing band gap energy. • The rate constant (k) of the degradation of acetone under visible light was highest for the catalyst 0.05-Ru-TiO_2. • The total pore volume and a pore radius of	[95]

						3.1 eV for 0.05g-Ru-TiO_2; 3.1 eV for 0.01g-Ru-TiO_2 and 3.15 eV for 0.005g-Ru-TiO_2	catalyst increased with increasing content of Ru ions in the TiO_2 lattice. • Ru-doped TiO_2 catalyst structure was microporous with pore sizes in the range from 2 to 4 nm.	

T: Temperature
RH: Relative Humidity
AFR: Air Flow Rate
RT: Residence Time
NA: Not Available

Table 5. Summary of the common non-metal dopants in the TiO_2 photocatalyst with their operated photocatalytic conditions and maximum efficiencies.

Contaminant (Concentration)	Photocatalyst	Dopant	Experimental condition	Efficiency before doping	Efficiency after doping	Band gap	Remarks	Ref.
Toluene (40 ppm)	C-doped TiO_2; Support: dish	C	T=25±1 °C; RH=60%; Lamp: Xe-lamp, 150 W (λ>425 nm)	About 5%	About 58.5%	3.10 eV for TiO_2 and 2.30 eV for C-TiO_2-200 ºC	• C-TiO_2 at post-thermal temperature of 200 °C showed the higher activity. • The rate constant of the pseudo-first-order reaction of C-TiO_2-200 was 7.69×10^{-3} min^{-1} while for undoped TiO_2 was 0.49×10^{-3} min^{-1}. • The specific surface area of undoped TiO_2 and C-TiO_2-200 were 118.97 and 79.11 m^2/g, respectively. • Un-doped TiO_2 only absorbed the UV light, however, C-TiO_2 exhibited absorption of visible light.	[98]
Toluene (40 ppm)	C-doped TiO_2; Support: dish; Method: Hydrothermal	C 0.9, 2.1, and 3.4 wt.%	T=25±1 °C; RH= Controlled by a $CaCl_2$ dryer; Lamp: Visible light, 150 W, (λ>425 nm)	5.2% for undoped TiO_2 and 8.9% for P25 (after 2 h)	2.1 wt.% C-doped TO_2 81.8% (after 2 h)	3.10 eV for TiO_2; 2.97 eV for 0.9 wt.%-C-TiO_2; 2.90 eV for 2.1 wt.%-C-TiO_2 and 2.78 eV for 3.4 wt.%-C-TiO_2	• C-doped TiO_2 with 2.1 wt.% showed the maximum photocatalytic activity which considered as the optimum value for carbon doping in this study. • C-doping did not change the particles size and the crystal structure of catalysts significantly. • The TEM images for C-doped TiO_2 (2.1 wt.%) and undoped TiO_2 showed the mesoporous structure which consists of the huge amount of mono-dispersed particles with a size of nearby 10-12 nm. • C-doped TiO_2 catalyst was prepared by green synthesis method.	[38]

Toluene (100 ppm)	C- doped TiO_2; Support: optical fiber; Method: Sol-gel and dip coating (1 to 5 times coating, the film thickness of TiO_2 was 1.6, 2.6, 3.2, 4.0, 4.2 µm)	C 0.2 g carbon particle (with average diameter less than 50 nm)	T=25 °C; RH=30%; AFR= 3 L/min; Lamp: Hg lamp, (300 nm, 405 nm, 436 nm)	35-79% (during 0.5 min to 30 min)	62-94% (during 0.5 min to 30 min)	Calculated band gap: 3.07 and 2.85 eV for N -TiO_2	• Photodegradation efficiency was enhanced as the TiO_2 thickness film was increased from 1.6 µm to 3.2 µm. However, by increasing thickness over 3.2 µm, the efficiency was decreased as the excessive film layer prevented UV light from passing through the TiO_2 film. • The specific surface area for TiO_2 film (thickness 3.2 µm) was 55 m^2g^{-1} and for C-TiO_2 was 230 m^2g^{-1} • By-products were formic acid and ethyl ester.	[97]
Toluene (66.3 ppm)	C-doped TiO_2 and Degussa P25; Support: dish; Method: Hydrothermal	C	T=25±1 °C; RH=NA; Lamp: Xe lamp, 150 W	Efficiency NA [Rate constant k= 0.0008 min^{-1}]	Efficiency NA [Rate constant k= 0.0037 min^{-1}]	NA eV for P25; 2.80 eV for C-TiO_2-500 °C and 2.90 eV for C-TiO_2-600 °C	• The PCO of toluene followed the pseudo-first-order reaction. • The average diameter of the TiO_2 hollow spheres after calcination at 500ºC for 1 hr was 0.5-3.0 μm. • Degussa P25 exhibited lower activity rather than C-doped TiO_2. • The superior activity of C-doped TiO_2 at 500 °C resulted of the crystal structure and the mesoporous microstructure. • The band gap of the C-doped TiO_2 was narrower than that of the pure TiO_2.	[99]
BTEX (0.03 to 3.1 ppm)	S-doped TiO_2 and Degussa P25; Support: glass	S Molar ratio Titanium isopropoxide/thiourea was 1:4	T=19-25 °C; RH=10-20, 50-60, and 80-90%; AFR=0.5-6.0 L/min; Lamp: Fluorescent Visible light, 8 W (400-700 nm); Intensity= 1.9 $mWcm^{-2}$	About 5% for Benzene; 14% for Toluene; 13% for Ethylbenzene; 11% for m,p-Xylene and 13% for o-Xylene	About 41-1.3% for Benzene; about 85-1% for Toluene; about 97-13% for Ethylbenzene; about 97-53% for m,p-Xylene and about 95-51% for o-Xylene (in the range of 0.03 ppm to 3.1 ppm)	Calculated band gap: 3.11-1.73 eV for S -TiO_2	• By increasing the AFR from 0.5 to 6 L/min, the degradation of BTEX decreased, thus, for the lowest AFR, the decomposition efficiency was maximum. • The degradation efficiency of toluene and benzene exhibited a great dependency on RH and the decomposition efficiency of it increased by decreasing the relative humidity. • The efficiency of Ethylbenzene and m,p-xylene decomposition exhibited a less dependency on RH and almost equal for both 10-20% and 50-60%. Then the efficiency decreased by increasing the RH to 80-90%. • The degradation efficiency of BTEX exhibited an increasing trend with decreasing initial concentration because of competitive adsorption between pollutant molecules on the photocatalyst surface.	[65]

BTEX (0.1, 0.5, 0.7, and 0.9 ppm)	S-doped TiO_2; Support: Aluminum sheet	S/Ti ratio: 0.2, 0.4, 0.8, and 1.6	T=NA; RH= 45%; AFR=1, 2, 3, and 4 L/min; RT= 2, 2.6, 3.9, and 7.8 s; Lamp: Daylight (8 W); Intensity= 2.8 $mWcm^{-2}$	TiO_2-AS About 2% for Benzene; 11% for Toluene; 21% for Ethylbenzene; and 36% for Xylene	For S-TiO_2-0.8-AS about 34% for Benzene; about 78% for Toluene; about 91% for Ethylbenzene; and about 94% for Xylene	3.02 eV for TiO_2 and 2.75 eV for S-TiO_2-0.8-AS	• The photocatalytic degradation efficiencies of BTEX under visible irradiation enhanced with increasing S/Ti ratios from 0.2 to 0.8, then decreased when the ratio increased to 1.6. • The photocatalytic degradation efficiencies of all target compounds over S-TiO_2-0.8-AS decreased with increasing air flow rate. • The XRD of both S-TiO_2-0.8-AS and TiO_2-AS samples showed an anatase crystal structure with a major band at 2θ= 25.2° and a rutile crystal structure with a major band at 2θ = 27.4°. • The photocatalytic degradation efficiencies showed an increasing pattern with decreasing initial contaminant concentration.	[101]
BTEX (100 ppb)	N-doped TiO_2 and Degussa P25; Support: Pyrex	N	T=19-25 °C; RH=10-20, 50-60, and 80-90%; AFR=0.5,1.0, and 2.0 L/min; RT= 22, 11, and 5.5 s; Lamp: Fluorescent visible light, 8 W (400-700 nm); Intensity= 1.9 $mWcm^{-2}$	About 14% for Benzene; 17% for Toluene; 16% for Ethylbenzene; 12% for m,p-Xylene and 17% for o-xylene	About 24% for Benzene; about 64% for Toluene; about 93% for Ethylbenzene; about 96% for m,p-Xylene and about 91% for o-Xylene (AFR=0.5 L/min, RH=50-60%)	Calculated band gap: 3.11-1.73 eV for N -TiO_2	• For all three examined flow rates, the PCO degradation efficiency for ethyl benzene and o,m,p-xylenes were higher than that of toluene or benzene. • The PCO degradation efficiency of all target compounds increased as the flow rate decreased. • Benzene exhibited the lowest degradation. • Increasing the distance of the catalyst from the light source led to the decrease in the light intensity in the reactor and caused a drop in the degradation efficiency of the target compounds.	[39]
Toluene (500 ppm)	N-doped TiO_2, undoped TiO_2, A-287, PC105, DegussP25, and PC103; Support: Pyrex	N N/Ti molar ratio of 6.6, 7.6 and 9.2	T=NA; RH=60 %; Lamp: Solar lamp, 300 W (380-600 nm); Intensity= 1.2×10^{-5} Einstein dm^{-3} s^{-1}	13.7% for T9 (undoped TiO_2 at pH=9) 55.8% for A-287, 47.7% for PC105, and 56% for P25	79.6% for TN9 (prepared at pH=9)	Calculated band gap: 3.27-2.07 eV for N -TiO_2	• The reaction kinetics for all synthesized catalyst could be explained as a pseudo-first-order rate equation. • The N-doped TiO_2 (prepared at pH=9 has the fastest kinetics constant which value is k = 6.0×10^{-3} min^{-1}	[24]
Acetaldehyde (600–3650 ppm)	N-doped TiO_2; Method: Thermal treatment	N	T=25 ºC; RH=NA; AFR=1000 mL/min;	88.1% for 600 ppm; 77.3% for 1000 ppm;	100% for 600 ppm; 92.1% for 1000 ppm;	3.16 eV for P25 and 2.91 eV for N-TiO_2	• The absorption range of N-doped TiO_2 photocatalyst was expanded to the visible range.	[100]

			Lamp: High pressure Hg lamp, 80 W (185–580 nm)	66.1% for 1700 ppm; 58.8% for 2200 ppm; and 51.2% for 3650 ppm	87.2% for 1700 ppm; 81.2% for 2200 ppm and 77.6% for 3650 ppm			
Toluene (NA)	B-doped TiO_2; Support: Pyrex; Method: Sol-gel	Br: 1, 3, and 5 wt.%	T=70 ℃; RH=NA; Lamp: UVC (10 W, 254 nm) and halogen (150 W,400 nm)	92 %	About 100% for B-doped TiO_2	Calculated band gap: 3.11 eV for B-TiO_2	• All samples were pure anatase TiO_2 after calcination and no phase change happened during the doping process. • In XRD pattern, the crystallite size reduced with doping B into the TiO_2. • The most characteristic feature of B-doping was that both surface area and pore volume of TiO_2 were increased. • All reactions followed pseudo first- order kinetics.	[23]
Acetaldehyde (600–3650 ppm)	F-doped TiO_2; Method: Impregnation	F	T=25 ℃; RH=NA; AFR=1000 mL/min; Lamp: High pressure Hg lamp, 80 W (185–580 nm)	88.1% for 600 ppm; 77.3% for 1000 ppm; 66.1% for 1700 ppm; 58.8% for 2200 ppm and 51.2% for 3650 ppm	97% for 600 ppm; 81% for 1000 ppm; 76% for 1700 ppm; 68% for 2200 ppm and 62% for 3650 ppm	3.16 eV for P25 and 3.09 eV for F-TiO_2	• The F-doped TiO_2 catalyst exhibited a stronger light absorption in the UV region, but did not have any significant photoactivity in visible range. • The F-doped TiO_2 reduced the recombination process of charge carrier and led to the formation of new active sites. • The F-doped TiO_2 led to increase pollutants adsorption capacity and photocatalytic activity. • F-doped TiO_2 photocatalyst had less specific surface area compared to P25, which it indicates that crystals' growth was improved.	[100]

T: Temperature
RH: Relative Humidity
AFR: Air Flow Rate
RT: Residence Time
NA: Not Available

Table 6. Summary of the common co-doped TiO_2 photocatalyst with their operated photocatalytic conditions and maximum efficiencies.

Contaminant	Photocatalyst	Dopant	Experimental	Efficiency	Efficiency	Band gap	Remarks	

(Concentration)			condition	before doping	after doping			Ref.
Toluene (40 and 133 ppm)	N, C, and S tri-doped TiO_2; Support: dish	The molar ratio of Ti:R 1:0, 1:1, 1:2 and 1:3, (TCNS0, TCNS1, TCNS2 and TCNS3)	T=25±1 °C; RH=NA; Lamp: Xe-lamp, 150 W	Efficiency NA [Rate constant, k (min^{-1}) for P25= 6.95×10^{-2}]	Efficiency NA [Rate constant, k (min^{-1})= 12.8×10^{-2}]	3.18 eV for TCNS0; 3.0 eV for TCNS1; 2.88 eV for TCNS2 and 2.67 eV for TCNS3	• TCNS1 (R-doped TiO_2, R=1, Ti: R=1:1) showed the higher activity under UV-vis light irradiation. • The rate constant of the pseudo-first-order reaction of TCNS0, TCNS1 under UV-vis light were 5.54×10^{-2} min^{-1} and 12.7×10^{-2} min^{-1} respectively. • The specific surface area of TCNS0 and TCNS1 were 155.1 and 154.3 m^2/g respectively.	[72]
Formaldehyde (200±10 ppm)	N, C, and S tri-doped TiO_2 and P25	N, C, and S. The molar ratio of thiourea to TiO_2 was 0, 1, 2, 3 and 6	T= Ambient temperature; RH=NA; Lamp: daylight (420 nm); Intensity= 0.46 ± 0.01 $mWcm^{-2}$	2% for undoped TiO_2 and 5% for P25	32.6% for N, C, and S-doped TiO_2-3	3.0 eV for P25; 3.2 eV for TiO_2; 2.8 eV for N-C,S-TiO_2-1; 2.5 eV for N-C,S-TiO_2-2; 2.4 eV for N-C,S-TiO_2-3 and 2.2 eV for N-C,S-TiO_2-6	• The tri-doped catalysts could be activated by visible light and more photogenerated charge carriers can be generated and participate in the photocatalytic reactions. • The C, N, S tri-doped TiO2 catalyst caused band gap narrowing and reduced the recombination of photo-generated charge carriers and thus enhanced photocatalytic activity.	[104]
Acetaldehyde (600–3650 ppm)	F and N co-doped; Method: Sol-gel	F and N	T=25 ºC; RH=NA; AFR=1000 mL/min; Lamp: High-pressure Hg lamp, 80 W (185–580 nm)	88.1% for 600 ppm; 77.3% for 1000 ppm; 66.1% for 1700 ppm; 58.8% for 2200 ppm and 51.2% for 3650 ppm	100% for 600 ppm; 98.2% for 1000 ppm; 94.1% for 1700 ppm; 87.1% for 2200 ppm and 80.7% for 3650 ppm	3.16 eV for P25 and 2.86 eV for F-N-TiO_2	• The absorption ranges of F and N co-doped TiO_2 photocatalysts was extended to the visible light. • The F and N co-doped TiO_2 catalyst had demonstrated the highest photocatalytic activity than other catalysts. • Doping both N and F ions caused synergy effects such a narrowing band gap, formation of new active sites and enhancement of photoactivity. • By increasing the initial contaminant concentration in the gas phase, the number of the available active sites of the catalyst became less than the amount of the pollutants. • The F and N co-doped TiO_2 photocatalyst had less specific surface area compared to P25, which it indicates that crystals' growth was improved.	[100]

Hexane and Butyl acetate (100 ppm each) and their mixture	Ag and V co-doped TiO_2; Support: polyurethane	Ag and V (0-6 wt.%)	T=NA; RH=50 %; AFR=100 mL/min; RT= 72s; Lamps: Two white light lamps, 20 W ($400<\lambda<700$); Intensity= 50 $mWcm^{-2}$	NA	Individual: 93.7% for Hexane and 95.5% for Butyl acetate In mixture: 75% for Butyl acetate and 48 % for Hexane	3.20 eV for TiO_2/PU; 3.02 eV for 6Ag/0V-TiO_2/PU; 2.91 eV for 5Ag/1V-TiO_2/PU; 2.86 eV for 4Ag/2V-TiO_2/PU; 2.79 eV for 3Ag/3V-TiO_2/PU; 2.77 eV for 2Ag/4V-TiO_2/PU; 2.81 eV for 1Ag/5V-TiO_2/PU and 2.83 eV for 0Ag/6V-TiO_2/PU	• The optimum catalyst (4Ag/2V-TiO_2/PU) had combination weight ratios of 4wt% Ag/TiO_2 and 2wt% V/TiO_2 led to the highest BET surface area of 230.5 (m^2/g). • The surface area of the co-doped photocatalyst was also higher than that of the undoped and single-dopant photocatalysts. • Due to the high polarity of butyl acetate, higher amount of butyl acetate was adsorbed on the surface of 4Ag/2V-TiO_2/PU than hexane.	[108]
Acetone (NA)	C and Mo co-doped TiO_2 and undoped TiO_2 (Degussa P25); Support: dish	Mo: 2 at. % and C: 1 at. %	T=NA; RH=NA; Lamp: UV lamp, 125 W and glass filter to produce visible light	53%	76.5%	Calculated band gap: 2.96 eV for C, Mo-TiO_2	• Doping a small amount of C had no obvious effect on the crystalline size, while, the crystalline size of the Mo-doped and co-doped samples were smaller than that of the undoped one. • C and Mo enhanced both the absorption ability of visible light and promoted the separation of photogenerated charge carriers. • The surface area and pore size of C, Mo co-doping TiO_2 significantly increase compared with those for P25.	[138]
Toluene (39.8 and 132.68 ppm)	Fe and N co-doped TiO_2	Fe: 0, 0.005, 0.02, 0.05, 0.1, 0.5, 1.0 and 2.0 wt.%	T=25±1 °C; RH= 60%; Lamp: Xe-lamp, 150 W	63%	Around 97%	Calculated band gap: 2.92 eV for Fe, N-TiO_2	• The optimum concentration of Fe ions was 0.02wt.% for the maximum photodegradation of toluene. • The Fe, N co-doped TiO_2 catalyst demonstrated about three times higher photoactivity than that of N–TiO_2 nanocrystals. • The reused Fe/N–TiO_2 photocatalyst did not demonstrate an apparent change in photocatalytic activity.	[120]
Toluene (NA)	B and Fe co-doped TiO_2; Method: Sol-gel	B: 3 wt.% Fe: 0, 0.5, 1, 3, and 5 wt.%	T=70 °C; RH=NA; Lamps: UVC (10 W, 254 nm) and halogen	Under Visible light About 8.8% (after	Under Visible light: About 87.9% (after 180 min)	Calculated band gap: 3.11-2.07 eV for B, Fe-TiO_2	• All samples were pure anatase TiO_2 after calcination and no phase change happened during the co-doping process. • In XRD pattern, the crystallite size reduced with	[23]

			lamp (150, 400 nm); Visible light emitting flux: 3.9×10^{-6} Einstein/s and UV light emitting flux: 1.47×10^{-6} Einstein/s	180 min)			doping B and Fe ions into the TiO_2 and the decrease of crystallite size was more result of B-doping than with Fe-doping. • All reactions follow pseudo first- order kinetics rate.	
Toluene (800 ppmv)	S and Fe co-doped TiO_2; Support: Pyrex	Fe: 1.5% S/Ti molar ration: 1% to 20%	T=Room temperature; RH=75%; AFR= 100 mL/min; Lamps: UVA and simulating sunlight, 6W for both	Efficiency NA [Reaction rate for P25 (mol/s.m^2): 3.87634×10^{-10}]	Efficiency NA [Reaction rate for S, Fe co-doped TiO_2 (mol/s.m^2): 4.77957×10^{-10}]	NA	• The S, Fe co-doped TiO_2 catalyst has improved photoactivity compared to the single-doped Fe-TiO_2 and P25 under both sunlight and UV-light irradiation. • The XRD patterns of both S, Fe co-doped, and S-doped TiO_2 were included 100% anatase crystal phase. • In the S, Fe co-doped TiO_2 catalysts, adding the S content led to a gradual increase of the BET surface area value and pore size. • All S, Fe co-doped TiO_2 catalysts showed great absorption in the visible light compared to the S-doped TiO_2 catalysts. • Generated by-product was benzaldehyde.	[87]

T: Temperature
RH: Relative Humidity
AFR: Air Flow Rate
RT: Residence Time
NA: Not Available

Table 7. Summary of the common semiconductor coupled TiO_2 photocatalyst with their operated photocatalytic conditions and maximum efficiencies.

Contaminant (Concentration)	Photocatalyst	Dopant	Experimental condition	Efficiency before doping	Efficiency after doping	Band gap	Remarks	Ref.
Propylene (NA)	$MnCO_3$ -TiO_2 and P25; Support: glass plate	$MnCO_3$/TiO_2 ratios: 1:10, 1.5:10, and 2:10	T=NA; RH=NA; RT=8 min; AFR=200 mL/h;	0% for $MnCO_3$, and 7% for P25	70%	Calculated band gap: 2.96 eV for $MnCO_3$ -TiO_2	• $MnCO_3$-TiO_2 (2:10) exhibited the highest activity for degradation of propylene. • The majority of $MnCO_3$ was nanoparticle (NP) with an average size of 4–5nm. • Comparing with P25 and $MnCO_3$, $MnCO_3$-TiO_2	[139]

			Lamp: Xenon lamp,500 W ($\lambda \geq 420$ nm); Intensity= 25 $mWcm^{-2}$				represented high absorption in visible light, especially in 400–500 nm region.	
Hexane and Isopropyl alcohol (0.1 ppm for each)	N doped TiO_2-WO_3	$N/WO_3/TiO_2$ compositions: 2.5/0.5/100, 2.5/1.0/100, 2.5/2.0/100, 2.5/4.0/100, and 2.5/6.0/100	T=NA; RH=45%; AFR=0.1, 0.5, and 1 L/min; RT= 1.3, 0.26, and 0.13 min; Lamp: 8 W, 400-720 nm; Intensity= 0.48 $mWcm^{-2}$	4% for Hexane	WO_3-N-TiO_2-4 43.4(±1.1)% for pure Hexane, and 72.7(±1.6)% for pure IPA In mixture: 34.2(±1.5)% for Hexane and 72.6(±1.7)% for IPA	3.17 eV for TiO_2; 3.08 eV for N–TiO_2; 2.91 eV for WO_3–N–TiO_2-0.5; 2.83 eV for WO_3–N–TiO_2-1; 2.80 eV for WO_3–N–TiO_2-2; 2.78 eV for WO_3–N–TiO_2-4 and 2.75 eV for WO_3–N– TiO_2-6	• The photocatalytic degradation efficiency of the WO_3–N–TNS catalysts enhanced by increasing in WO_3 loading from 0.5% to 4.0%, while, a further increase in the WO_3 loading to 6.0% resulted decreasing in photocatalytic efficiency. • The deposition of WO_x species on the TiO_2 surface provided a higher surface area, however, the excess amount of WO_3 caused partial blockage the TiO_2 pores and led to the lower surface area. • The photocatalytic degradation efficiency for pure IPA was higher than that for pure hexane. • The photocatalytic degradation efficiency for hexane mixed with IPA, was lower than that for pure hexane, while the IPA decomposition efficiency remained relatively constant.	[106]
Toluene (NA)	Pt-SnO_2-R/TiO_2-A/TiO_2 and Titania nanotubes (TNT)	Sn/Ti ratio: 2(S1), 6(S2), 10(S3), 15(S4) at. % and P1 was S3 doped with Pt (1 wt.%)	NA	Efficiency NA [CO_2 production rate: 20.43 ppm/h]	Efficiency NA [CO_2 production rate: 113.81 ppm/h]	3.13 eV for Pt-SnO_2-TiO_2	• The anatase phase was observed in all photocatalysts. However, the rutile and SnO_2 appeared just for S3, S4, and P1 catalysts. • The specific surface area was in the order S0 < S3 < P1, demonstrating that the number of mesoporous structures existing in the photocatalysts increased the specific surface area. • S3 and P1 demonstrated larger pore volumes, pore diameters, more active site and better adsorption than TNT. • By increasing the Sn/Ti ratio to 10 at. % the photocatalytic efficiency was enhanced. However, by more increasing from 10 to 15 at.% the efficiency was decreased.	[22]
Toluene (177 ppm)	xNi- TiO_2-SnO_2; Method: Sol-gel and wet-impregnation	x=0.1, 0.3, and 0.5 wt% SnO_2: 1 wt%	T=70 °C; RH=NA; AFR=320 cm^3/min; Lamp: Halogen	5.7%	51%	Calculated band gap: 3.11 eV for Ni-SnO_2-TiO_2	• All reactions for all different catalysts followed pseudo first-order kinetics as the rate of reaction for certain amount of catalyst depends only on toluene concentration. • The rate constant for 0.3 wt% Ni–TiO_2–SnO_2 had the	[21]

			lamp, 150W; Visible light emitting flux: 3.9×10^{-6} Einstein s^{-1}				highest value (0.0058 min^{-1}) among the tested catalysts. • xNi-doped TiO_2 was active in visible light while a composite of SnO_2 onto the TiO_2 surface further increase the efficiency of these catalysts. • The Ni-doped TiO_2 nanoparticles host SnO_2 on their surface caused to reduce the recombination rate. • TiO_2 and TiO_2–SnO_2 catalyst were inactive under visible light irradiations	
Toluene (7 ppm)	SiO_2 doped TiO_2; Method: Sol-gel	Si/Ti molar ratio of 1:100, 5:100, 10:100, 15:100, and 20:100	T=NA; Humidity=1.6 g/m^3; Lamp: UVA mercury lamp, 300 W (365 nm)	69.6% for undoped TiO_2 and 70.5% for P25	90.6%	NA	• The 10% SiO_2 doped TiO_2 fibrous catalyst calcined at 400 ºC had the highest degradation rate compared to the other catalysts. • Based on the results 400°C was selected as the optimum temperature to remove organic compounds. • The surface area for SiO_2 doped TiO_2 ratio at 10% was 266 m^2/g.	[37]
Benzene (280 ppm)	Ag_3VO_4 -TiO_2 And pure TiO_2 (TiO_2 at cal. Temp:500 °C); Method: Hydrothermal	mass fraction of Ag_3VO_4 in nanocomposites was 0.1, 0.5, 1, 2, and 5 %,	T=30±1 °C; RH=NA; AFR= 20 cm^3/min; Lamps: Xe-arc lamp, 500 W (450<λ<900), and Xe-arc lamp, 500 W (λ<450)	Under visible light: 8.9% Under solar light: 43%	Under visible light: 40% Under solar light: 94.5%	Calculated band gap: 2.76 eV for Ag_3VO_4-TiO_2	• By increasing the amount of Ag_3VO_4 in Ag_3VO_4/TiO_2 nanocomposites, the anatase phase was increased. • 0.5% Ag_3VO_4 in nanocomposites catalyst presented optimum activity for benzene degradation under visible light irradiation. • The absorption edge and band gap of Ag_3VO_4 were estimated to be 560 nm and 2.2 eV. • By increasing the amount of Ag_3VO_4 till 2% the BET specific surface area of Ag_3VO_4/TiO_2 increased, and more increasing of that resulted in decreasing of the surface area. • The specific surface area for 0.5% Ag_3VO_4/TiO_2 nanocomposites and TiO_2 were determined to be 48.98 and 28.24 m^2g^{-1}, respectively.	[36]
Benzene (NA)	CdS-TiO_2; Support: fiber glass; Method: Sol-gel	Cd/Ti: 5.65, 7.93, 9.20, and 22.5 %	T=NA; RH=NA; Lamp: High-pressure mercury, 160 W	55.4% for TiO_2/FGC	92.8% for 5.65%-CdS / TiO_2-FGC under UV-vis and and 32.7% for 5.65%-CdS / TiO_2-FGC under	Calculated band gap: 3.11 eV for CdS-TiO_2	• By increasing the CdS amount, the photocatalytic activity of catalysts initially increased and then showed a downward trend. • All the catalysts with different amount of CdS under visible light irradiation showed greater photocatalytic activities than TiO_2-FGC. • The recombination rate of charge carriers in CdS-TiO_2 composite was effectively decreased.	[140]

					visible			
Benzene (31.3-62.6 ppb) and Toluene (26.54-53.07 ppb)	TiO_2 composite ZnO	50% TiO_2 and 50% ZnO	T=NA; RH=NA; AFR=0.42 - 2.54 L/min; RT=5−30 min; Lamp: UVA (365-400 nm); Intensity= 0.4, 0.6, and 1 $mWcm^{-2}$	NA	93% of Toluene and 78% of Benzene	Calculated band gap: 3.11 eV for ZnO-TiO_2	• The toluene and benzene degradation enhanced with increase UV light intensity in a different amount of catalyst and times. • The removal efficiency of benzene was less than that of toluene. • Toluene & benzene removal on TiO_2/ZnO catalyst under UV light followed by first-order kinetic reactions rate.	[141]
Benzene, Toluene, o, m and p-Xylene (BTX) (NA)	N doped TiO_2-Nb_2O_5 composite; Method: Sol-gel	N: 0.49 at.% TiO_2: 50 wt.% Nb_2O_5:50 wt.%	T=25±2 °C; RH=NA; Lamp: White LED (16 W) and Black (46 W)	78.5% for TiO_2 (UVA) 19% for TiO_2 (Vis)	p-Xylene: 97.5% for N-TiO_2, 84.6% for N-TiO_2/Nb_2O_5 (UVA) 62% for N-TiO_2, 56% for N-TiO_2/Nb_2O_5 (Vis)	3.18 eV for TiO_2-500 °C; 2.78 eV for N-TiO_2-500 °C; 3.28 eV for TiO_2-Nb_2O_5 -500 °C and 3.02 eV for N-TiO_2-Nb_2O_5 -500 °C	• The photo-oxidation reactions were followed pseudo first-order kinetics. • The N–Ti calcined at 500 ºC had the highest efficiency under UVA and visible light, with an apparent reaction rate constant of 0.0243 and 0.0076 min^{-1}, respectively. • According to results, the heterojunction of TiO_2 and Nb_2O_5 was not effective for the photocatalytic performance. • The anatase phase was detected in the TiO_2-Nb_2O_5 mixed catalysts. • Results showed that all the efficiencies of N-doped catalysts were better than its undoped TiO_2 catalyst.	[25]
Benzene, Toluene, and Xylenes (BTX) (100 ppm each)	N doped ZnO-TiO_2 composite; Method: Sol-gel	50 wt% of ZnO and 50 wt% of TiO_2	T=25 °C; RH=NA; Lamp: white LED, 16 W (439.8 nm);	NA	86% for Benzene, 87% for Toluene, and 86% for Xylene	NA eV for TiO_2 3.36 eV for ZnO-TiO_2-500 °C and 2.88 eV for N-ZnO-TiO_2-500 °C	• Doped photocatalysts exhibited higher specific surface area. • The presence of nitrogen led to control nucleation and growth of crystallites, as well as the formation of a well-order porous structure. • The N-doped TiO_2 had visible light absorption due to the interstitial doping. • The N-TiO_2-ZnO composite caused to photosensitize ZnO in visible wavelength region and reduce recombination rate of charge carriers. • The highest efficiency was achieved by N-TiO_2-ZnO calcined at 500 °C.	[105]

T: Temperature
RH: Relative Humidity
AFR: Air Flow Rate
RT: Residence Time

NA: Not Available